Original Paper

Landslides
DOI 10.1007/s10346-021-01813-3
Received: 12 July 2021
Accepted: 1 December 2021

Lingfeng He · John Coggan · Doug Stead · Mirko Francioni · Matthew Eyre

Modelling discontinuity control on the development of Hell's Mouth landslide

Abstract This paper focuses on numerical modelling and back analysis of the Hell's Mouth landslide to provide improved understanding of the evolution of a section of the north coast of Cornwall, UK. Discontinuity control is highlighted through the formation of a 'zawn' or inlet, the occurrence of two successive landslides and evidence of ongoing instability through opening of tension cracks behind the cliff top. Several integrated remote sensing (RS) techniques have been utilised for data acquisition to characterise the slope geometry, landslide features and tension crack extent and development. In view of the structural control on the rock slope failures, a 3D distinct element method (DEM) code incorporating a discrete fracture network and rigid blocks has been adopted for the stability analysis. The onset and opening of tension cracks behind the modelled slope failure zones has also been studied by analysing the displacements of two adjoining landslide blocks, between which, a joint-related tension crack developed. In addition, a sensitivity analysis has been undertaken to provide further insight into the influence of key discontinuity parameters (i.e. dip, dip direction, persistence and friction angle) on the stability of this section of the coastline. Numerical modelling and field observations indicate that block removal and preferential erosion along a fault resulted in the formation of the inlet. The development of the inlet provides daylighting conditions for discontinuities exposed on the inlet slope wall, triggering the initial landslide which occurred on 23rd September 2011. Numerical modelling, and evidence from a video of the initial landslide, suggests that the cliff instability is characterised by a combination of planar sliding, wedge sliding and toppling modes of failure controlled by the discrete fracture network geometry.

Keywords Coastal landslides · Remote sensing · 3D distinct element modelling · Discontinuity · Sensitivity analysis

Introduction

Discontinuities (such as joints, cleavages, bedding, foliation, faults and folds) produce weak planes in a rock mass that may contribute to the occurrence of landslides under unfavourable conditions associated with orientation, size, intensity and strength of discontinuities (Hutchinson 1989). Discontinuities can also behave as release surfaces at varying scales, along which failures can occur, allowing for sliding/fall from the main slope. There are numerous examples of discontinuity control on slope instability at varying scales in the literature. For example, the upper part of the La Valette landslide was shown to be structurally controlled at a regional scale with an estimated failure volume of 500,000 m^3 (Travelletti et al. 2013). Weidinger et al. (2014) noted that the occurrence of catastrophic landslides is likely related to relatively large-scale structures (e.g. tectonic faults). The gigantic 1999 Chiu-fen-erh-shan landslide developed along a pre-existing bedding fault that was formed during flexural slip folding, and its development was significantly influenced by the properties of the discontinuities (Wu et al. 2005). Inherited structures associated with slope-scale folding in Eastern Switzerland controlled the extent and mechanism of an on-going deep-seated gravitational slope deformation with a volume of 1.85 km^3 (Agliardi et al. 2019).

Further examples of discontinuity-controlled instability include the 2010 Qiyangou landslide that involved a wedge-planar failure where the failed rock mass was displaced along a basal surface and was bounded by discontinuities (i.e. a thrust fault and a series of aligned joints belonging to the same set) (Fan et al. 2019). A recent earthquake-induced massive landslide (2017) in China occurred in a complex geological environment where two active faults intersected to form a compressive stress concentration zone, with the interface between metamorphic sandstone and slate allowed sliding of the rock mass (Shao et al. 2019). Donati et al. (2019, 2020, 2021a, b) used a combined remote sensing (RS) and numerical modelling approach to highlight the importance of faults and shear zones in controlling the failure mechanisms at the Hope Slide, BC, the Downie Slide, BC, and the San Leo Rockslide, Italy. At a smaller scale, toppling failure that occurred in a granite slope of the Melbur Pit was shown to be controlled by unfavourably oriented discontinuities (Vanneschi et al. 2019).

Different methods have been used for the analysis of slope instability or landslides in jointed rock masses. Kinematic analysis provides a preliminary estimation of kinematic potential of a rock slope prone to different mechanisms of instabilities within the rock mass (i.e. planar sliding, wedge sliding and toppling) (Hoek and Bray 1981; Stead and Wolter 2015; Francioni et al. 2018b). For relatively simple scenarios, limit equilibrium methods are usually adopted and can consider potential influences such as pseudo-static, earthquake acceleration, groundwater conditions and anisotropy. They can determine the factor of safety depending on an assumed failure mode (Huang and Yamasaki 1993). In more complicated situations, 2D/3D numerical modelling methods can provide a comprehensive understanding of the stability conditions and mechanical behaviour of the slope, and allow simulation of progressive displacement and/or deformation involving the unstable slope prior to collapse (Jing 2003; Stead et al. 2006). In the context of jointed rock slopes, discontinuum modelling methods offer a significant advantage in modelling deformable or rigid body movements by treating the rock slope as a discontinuous rock mass. The simulated rock mass comprises an assemblage of deformable or rigid blocks, with defined structural-related contacts between them. Among discontinuum methods, distinct element methods (DEM)

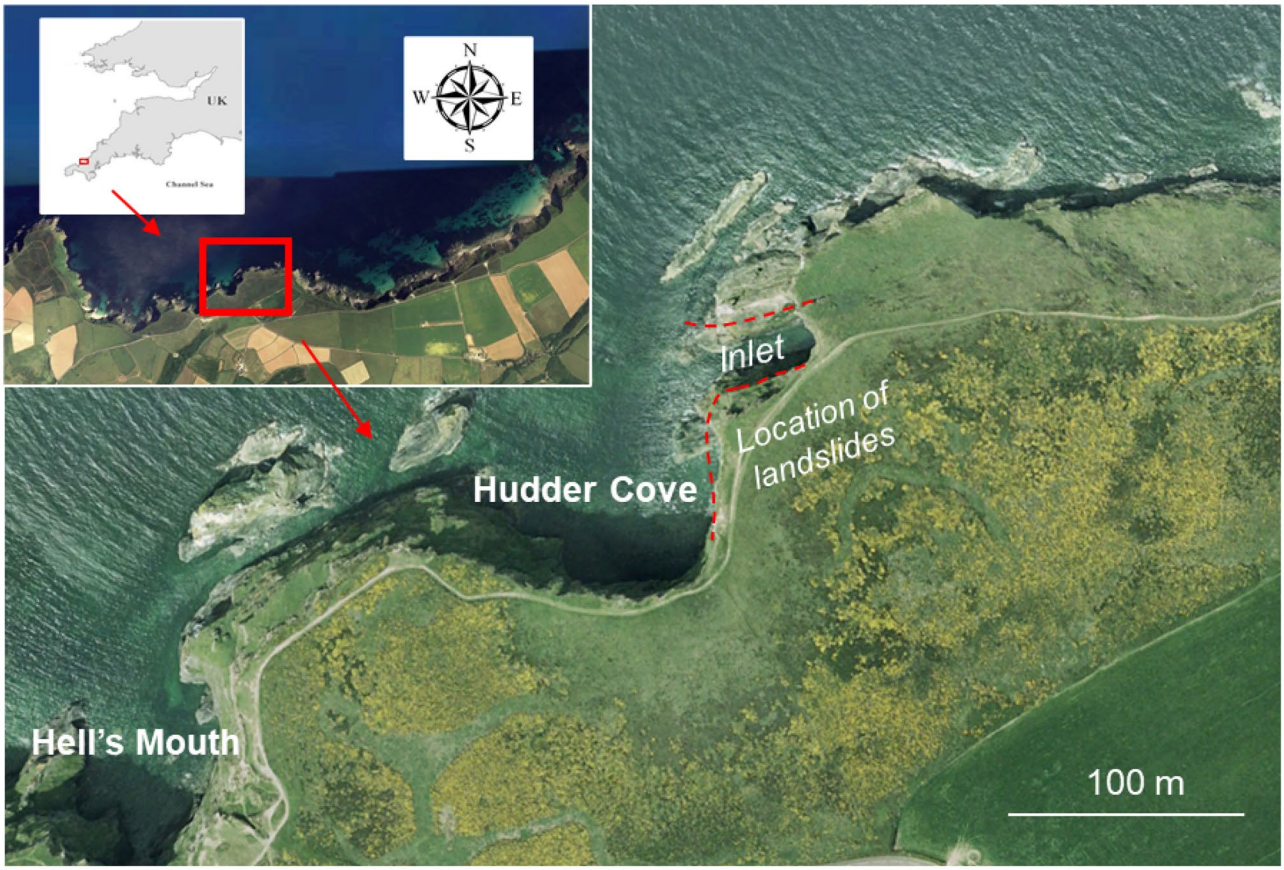

Fig. 1 3D Google Earth image in 2001 showing the location of the study area which is close to Hell's Mouth on the north coast of Cornwall, UK

(Corkum and Martin 2004; Brideau et al. 2007, 2011; Dong et al. 2018; Agliardi et al. 2019) and discontinuous deformation analysis (DDA) (Kveldsvik et al. 2009; Huang et al. 2016; Liu et al. 2019; Xia et al. 2021) are two frequently adopted approaches for the analysis of structurally controlled landslides.

Where landslides have occurred in a rock mass, discontinuities are usually related to the propagation of tension cracks (Bovis and Evans 1996; Brideau et al. 2007; Zhang et al. 2018). Brideau et al. (2007) found that the onset of tension cracks in the Dawson City landslide was related to the pre-existing discontinuity sets, where the distribution of tension cracks could be used for defining areas of unstable ground. Zhang et al. (2018) showed that interpreting tension cracks developed along a series of aligned joints contributed to defining the boundary of the landslide. Therefore, the analysis of visible tension cracks may be beneficial to the interpretation of discontinuities as well as providing further understanding into the development of a landslide. However, the onset and opening of tension cracks, has to date had limited consideration in numerical analysis of a landslide. A virtual joint was introduced by Wang et al. (2021) to simulate the propagation of cracks in intact rock masses in a 2D DDA (discontinuous deformation analysis). A 2D discrete element model was used to understand crack initiation, propagation and coalescence within a rock mass during an earthquake-induced rock avalanche (Gao et al. 2020). A simplified geometry of joints was used in a 3D distinct element simulation using 3DEC (Itasca Consulting Group, Inc. 2017), to investigate the displacement of rock masses along the joints forming the tension cracks (Corkum and Martin 2004).

In this paper, numerical modelling and back analysis of the Hell's Mouth landslide are used to provide improved understanding of the evolution of a section of the north coast of Cornwall, UK. The modelling uses a 3D distinct element approach that includes a representative discrete fracture network. The analysis provides

Table 1 Characteristics of 5 discontinuity sets and faulting identified by Francioni et al. (2018a), including dip, dip direction and associated descriptions of surface conditions

Discontinuity	Dip (°)/dip direction (°)	Bedding/joint description
S0	18/142	Bedding. Smooth, undulating, planar
J1/F1	34/320	Rough, undulating, stepped
J2/F2	87/336	Smooth, undulating, planar
J3/F3	64/143	Rough, undulating, planar
J4/F4	87/069	Smooth, undulating, planar

further insight into the formation of an inlet and the influence of the discontinuities on the landslide and subsequent tension crack formation behind the cliff crest. The modelling results have been verified by observations obtained from remote sensing (RS) surveys and evidence from analysis of a video taken of the initial landslide. A sensitivity analysis has also been undertaken to demonstrate the effects of key discontinuity parameters (i.e. dip, dip direction, persistence and friction angle) on the modelled landslide behaviour. This paper provides further insight into coastal evolution in blocky rock masses that are susceptible to discontinuity-controlled instabilities.

Study area description

The study area is located close to Hell's Mouth (Fig. 1), on the north coast of Cornwall in the southwest of England, UK. At this location, two successive landslides occurred in 2011 within a 3-month period. The area experiences a warm and temperate climate with average yearly temperature of 10 °C and average annual rainfall of 1062 mm. The cliffs in the vicinity of Hell's Mouth have an average height of approximately 70 m. The landslides occurred on the eastern side of a V-shaped cove (Hudder Cove which is directly east of Hell's Mouth). The eastern end of the V-shaped cove is characterised by a north–south striking near vertical scarp. An east–west fault-controlled striking 'zawn' is present at

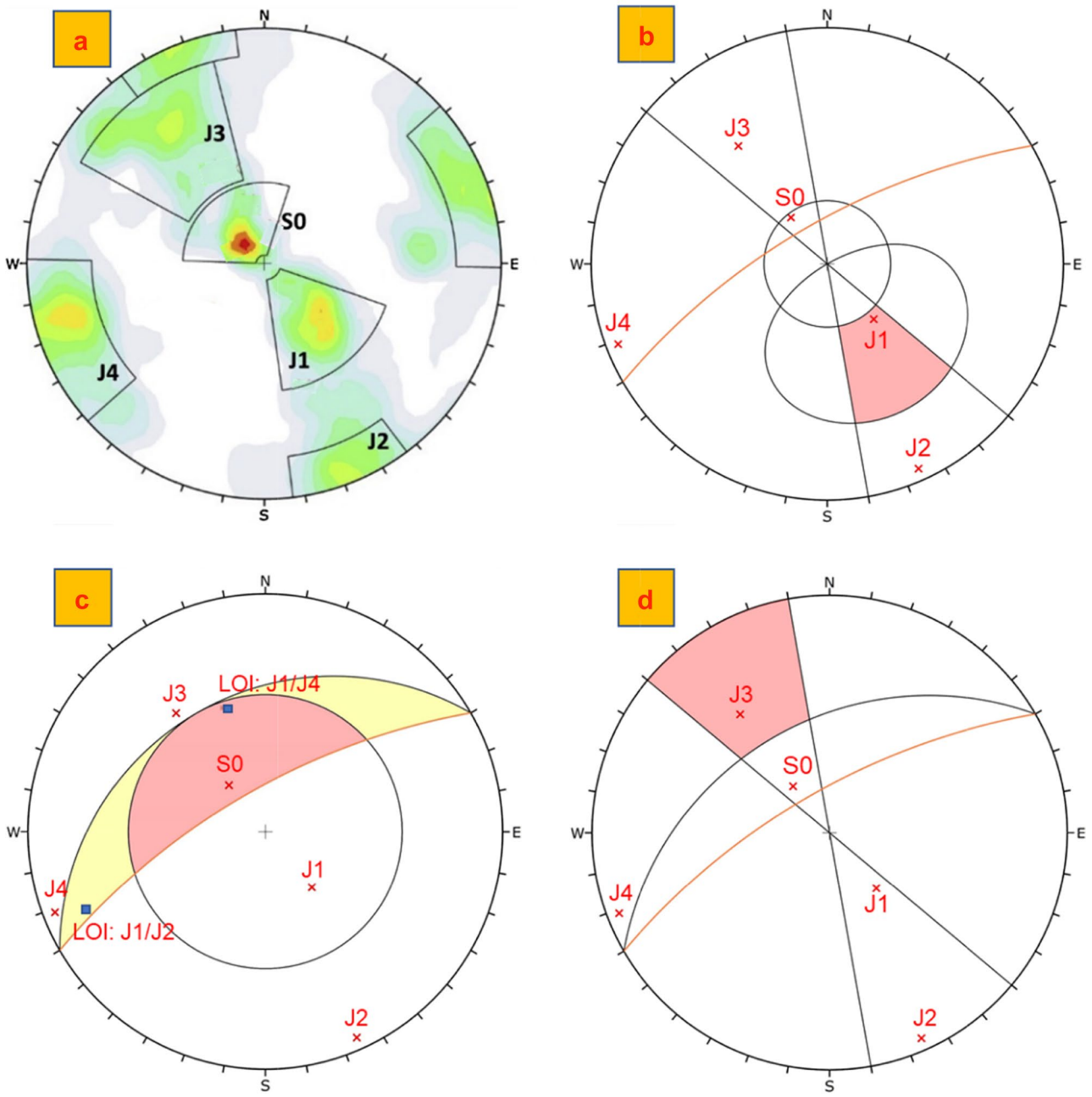

Fig. 2 **a**) Lower hemisphere stereonet showing contours of joint poles and 5 joint sets identified in the study area (Francioni et al. 2018a, **b**) kinematic overlay for planar sliding in the cliff (70°/330°) using the mean sets identified in part (**a**) and Table 1, **c**) wedge sliding kinematic analysis, **d**) flexural toppling kinematic analysis.

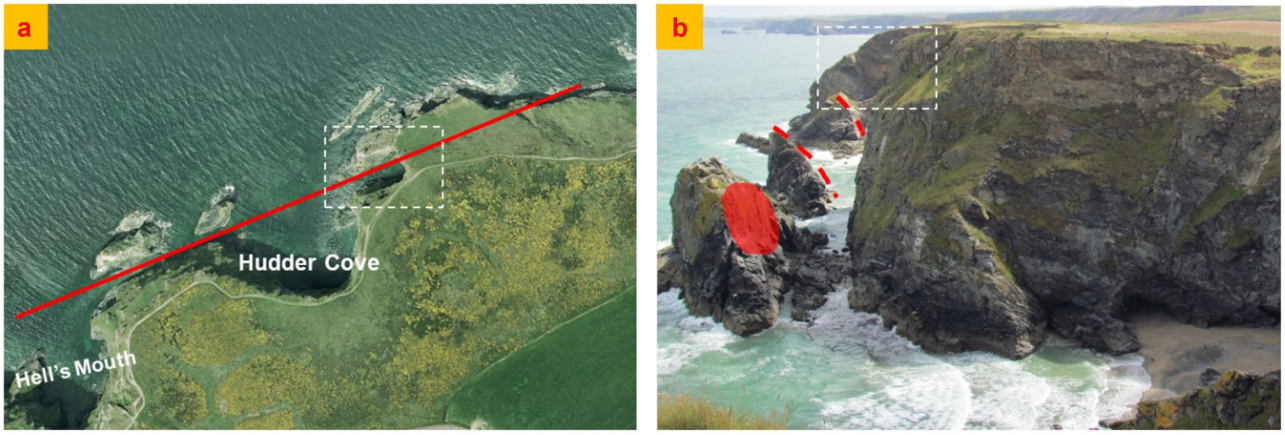

Fig. 3 **a**) 2001 Google Earth image (plan view) showing that a fault of system F3 (red line) has influenced development of stacks at the northern edge of Hell's Mouth and inlet formation in the study area (white rectangle zone), **b**) image taken from the west flank of Hell's Mouth looking towards east, showing the geomorphology of the 70-m-high cliff and fault-related (F3) scarps highlighted in red

the northern edge of the cove (it is referred as 'inlet' in Fig. 1). A 'zawn' can be described as a deep and narrow sea-inlet in the British Isles, especially Cornwall and the south-west, cut by erosion into sea-cliffs, with steep or near vertical sidewalls. In addition, shallow caves can be observed at the toe of the cliff which suggests that the slope is susceptible to sea erosion or block removal by wave attack.

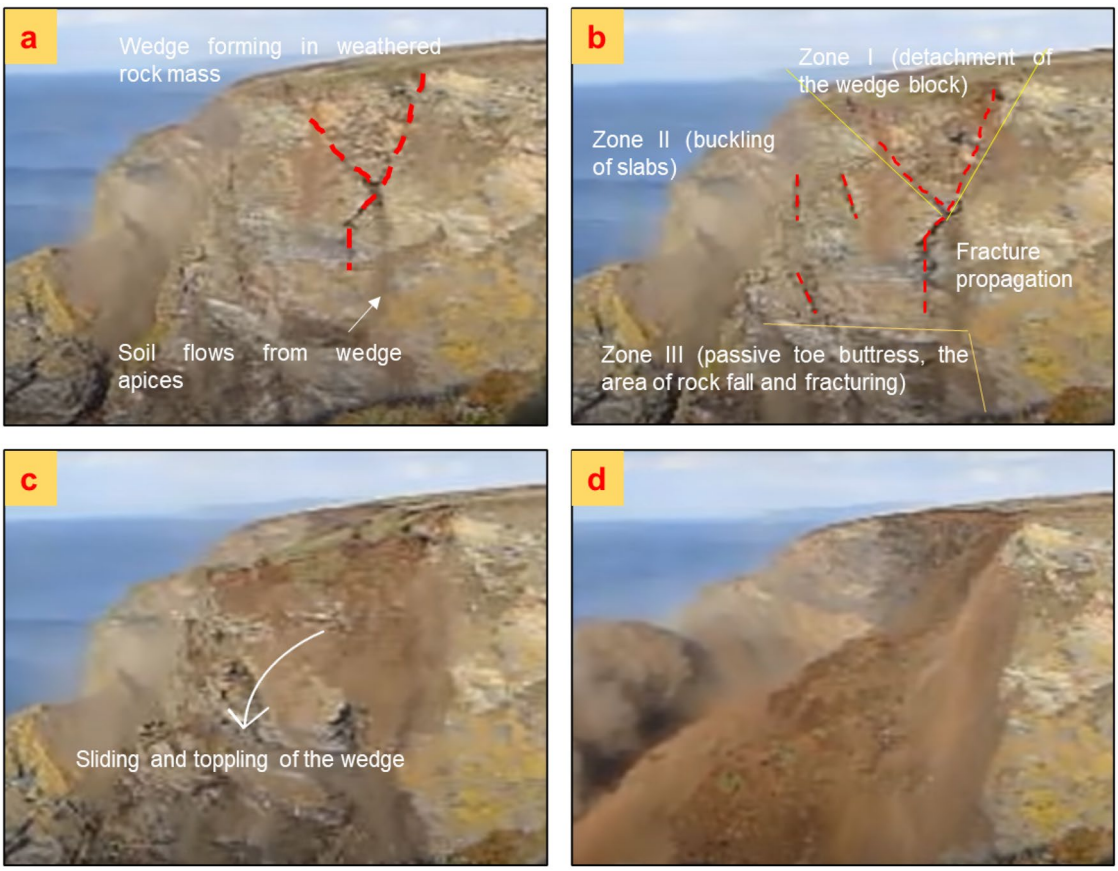

Fig. 4 Preliminary video-frame analysis of the initial landslide at Hell's Mouth from Stead (2021), with images looking towards east

Geological setting

The geology of the study area is dominated by the Porthtowan Formation (Gramscatho Group) (Leveridge and Shail 2011), which comprises of alternating beds of strong to moderately strong, medium to thinly bedded dark grey mudstone, interbedded with strong to moderately strong, thick to thinly bedded pale grey fine sandstone, which may locally have a silt and mud component (Hollick et al. 2006; Francioni et al. 2018a).

Five discontinuity sets have been previously recognised by Francioni et al. (2018a) over the study area through interrogation of point cloud data provided by remote sensing techniques (Fig. 2a and Table 1). The identified sets mainly follow two trends (north-west-southeast and northeast-southwest) and significantly contribute to the geological evolution of the area, as the trends of the coastline closely follow these directions (Francioni et al. 2018a). Bedding (S0) is slightly inclined and has the highest persistence among the identified discontinuity sets. Joints associated with set J3 have a dip direction parallel to the bedding but are more steeply inclined. Joint sets J2 and J4 are sub-vertical and have a dip direction sub-orthogonal to each other. Joint set J1 has the lowest persistence of the mapped discontinuities, and is sub-parallel to J2. J1, however, dips towards the north-west and therefore has the potential to form a basal surface for planar sliding that daylights in the cliff face. Importantly, field mapping and previous analysis of remotely captured point cloud data indicate that major fault systems (F1, F2, F3 and F4) are associated with the joint sets (as introduced in Table 1). The location and presence of these features dictate the potential for cliff instability and are directly associated with previous landslide activity within the immediate section of coastline (Francioni et al. 2018a). The listric fault F1, for example, is frequently associated with major planar and wedge failures along the coastline and has formed the basal feature of previous coastal landslides.

Using mean values of each identified joint set orientation and an initial friction angle of 30°, preliminary kinematic analysis associated with planar sliding (Fig. 2b), wedge sliding (Fig. 2c) and flexural toppling (Fig. 2d) was undertaken. This analysis indicates that the north-western facing sidewall of the 'zawn' or inlet with an orientation (70°/330°) has the potential to fail through planar sliding controlled by J1, wedge sliding dominated by intersections of J1/J4 and J1/J2 and flexural toppling associated with J3. An evaluation of the potential variation of discontinuity set orientations suggests that direct and oblique toppling may also be possible, resulting from basal planes formed by J1 and steeply inclined block edges formed by intersections of J2/J4 or J3/J4.

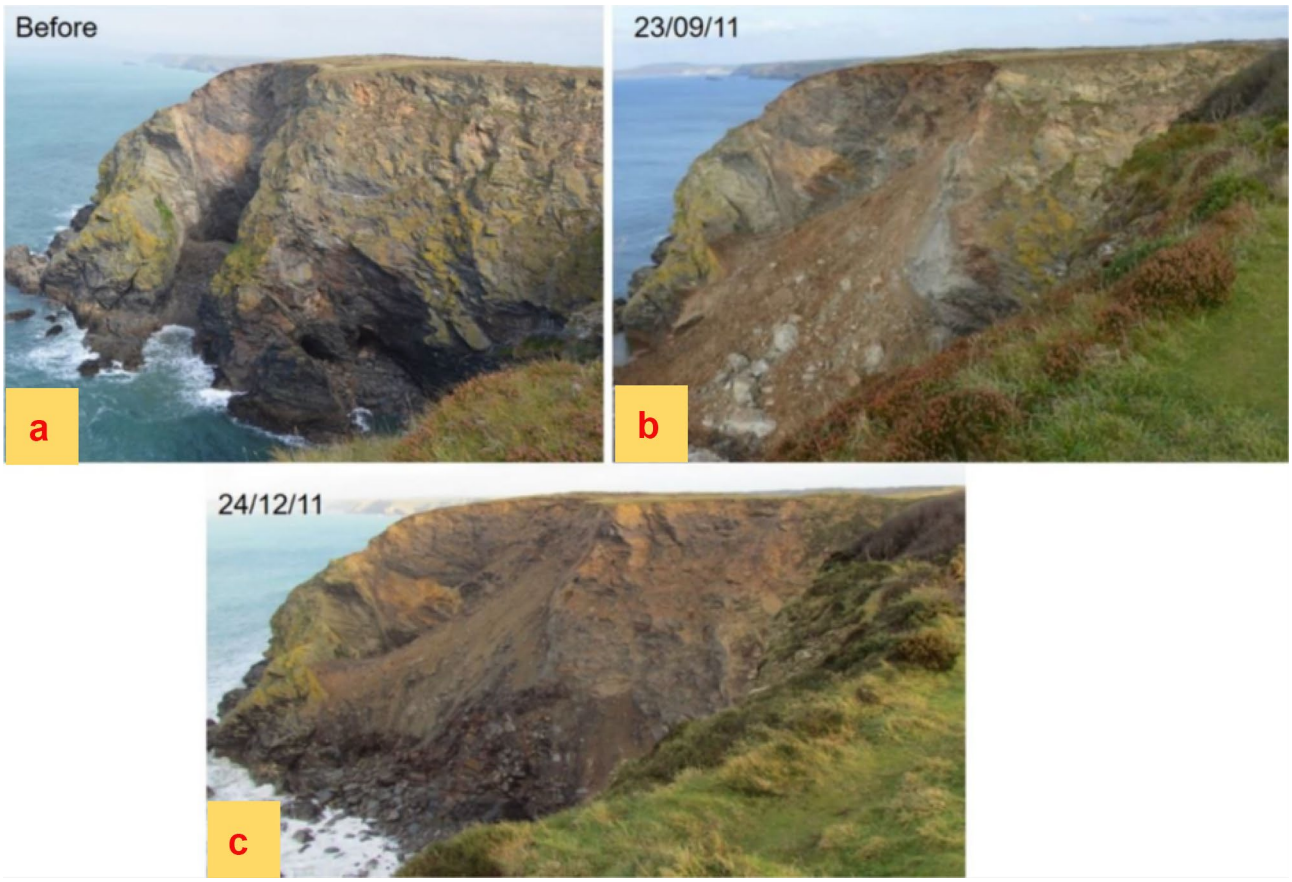

Fig. 5 Pre-landslide and post-landslide images obtained from Francioni et al. (2018a), showing the geomorphology of the analysed slope looking towards east at different time periods, **a**) prior to the landslide, **b**) after the first landslide episode, **c**) after the second landslide episode

Inlet formation

The north-east south-west trending fault (associated with F3) highlighted in Fig. 3a is identified as a major feature in the local geology of the area (Digimap 2020). It has a critical influence on the cliff orientation and geomorphology of the immediate area. Figures 3a and b show resulting stacks created at the northern edge of Hell's Mouth and the influence of the fault on inlet formation in the study area. Preferential erosion due to wave action, block release and erosion-induced caves can be observed at the toe of the cliff along this section of coastline (Fig. 3b). The cliff geomorphology prior to and after the two landslide events can be seen in Figs. 4 and 5. Two fault-related surfaces (70°/330° and 75°/160°) associated with F2 and F3 form the edges of the inlet. The discolouration of the rock within the vicinity of the inlet suggests an alteration zone that may be more susceptible to preferential erosion.

Previous landsliding activities

This section of coast is susceptible to landslides of various sizes (Shail et al. 1998; Francioni et al. 2018a; He et al. 2021). A significant landslide episode was videoed by engineers from Cornwall Council on the afternoon of Friday 23 September 2011 and is part of the British Geology Survey landslide database (British Geological Survey, 2020).

A video-frame analysis of the failure undertaken by Stead (2021) is provided in Fig. 4. Prior to major failure, initial development of wedge fractures, opening of fractures and soil flows were evident

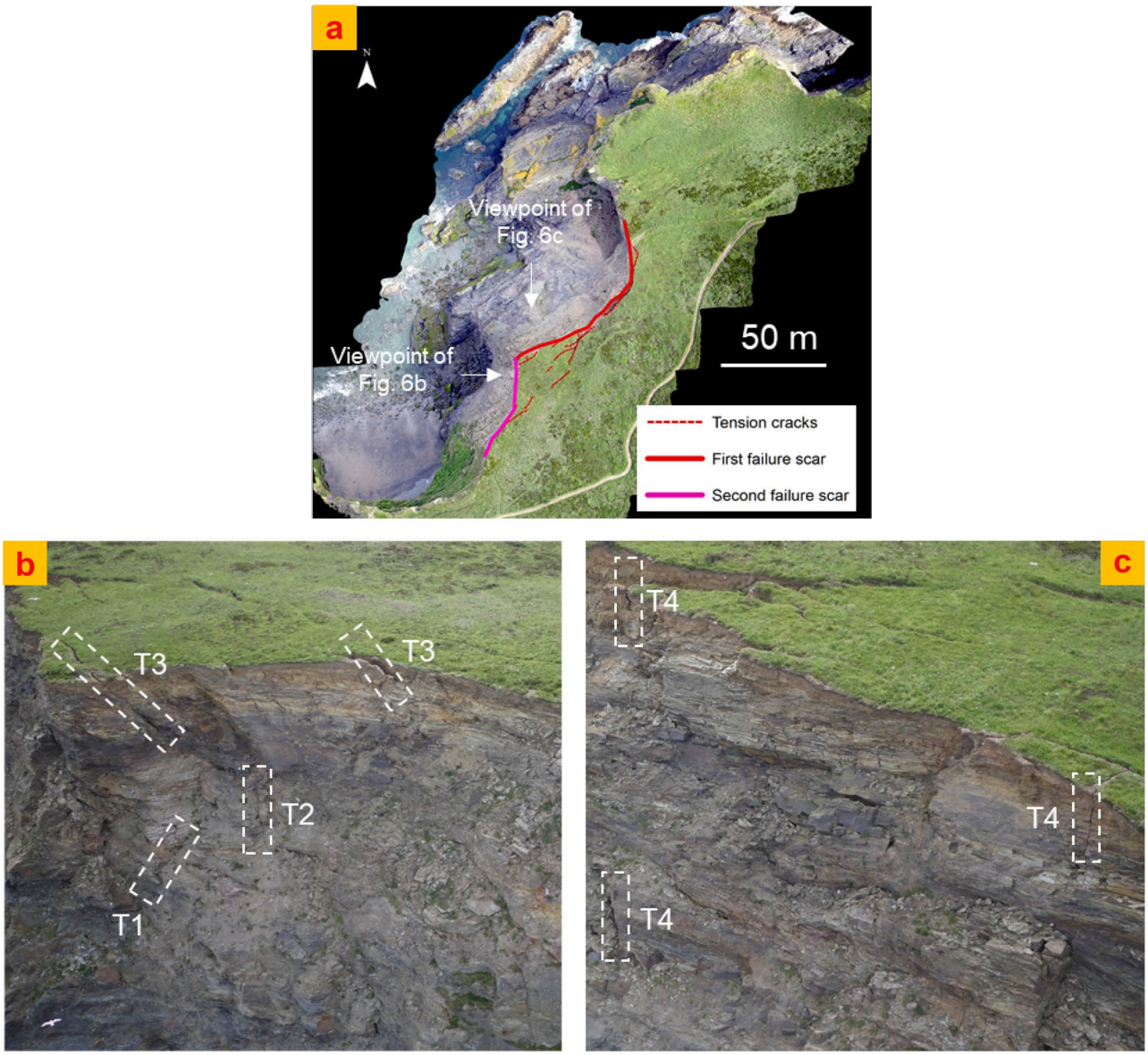

Fig. 6 Images of the post-failure slope at Hell's Mouth: **a**) an orthoimage showing landslide scars of the two failures and tension cracks behind the scars; **b**) an UAV image presenting tension cracks that daylighted at the slope surface looking towards east; **c**) tension cracks in slope face looking towards south

from the cliff face (Fig. 4a). This was followed by further fracture propagation, buckling of slabs and formation of an active–passive wedge near the toe of the slope (Fig. 4b). The fractures appear to propagate along pre-existing discontinuity orientations. Further sliding and wedge detachment occurs, with subsequent breakup of the rock mass during failure. The video shows the potential control of discontinuities on the propagation of the landslide.

Following the first landslide detailed above, in September 2011 a second landslide occurred immediately to the south of the first landslide, prior to a visit to the site by the second author in October 2011. The slope geometries prior to the two landslide episodes, after the first episode, and after the second episode have been presented in Fig. 5. It can be seen from Fig. 5c that the extent of the second slide was smaller than the first. The extents of landslides are also shown in plan view in Fig. 6a.

Post-landslide features

In view of the lack of safe access, remote sensing techniques were used to detect and characterise post-landslide features. Francioni et al. (2018a) reported initial use of terrestrial LiDAR and photogrammetry to generate three-dimensional point clouds for extraction of discontinuity orientation data and comparison of aerial LiDAR data for estimations of slide volumes. More recent analysis in June 2018 used a Panasonic DMC-GH4 camera mounted on an DJI M600 UAV to capture overlapping stereo photographic images (resolution: 4608 × 3456). These images were georeferenced using eight ground control points (GCPs) derived from 180 corrected observations using a Trimble R10 RTK GNSS that provided an accurate model to detect landslide features, including landslide scars and tension crack development behind the crest of the cliff.

Figure 6a presents an orthoimage constructed using the Metashape software (Agisoft 2016) from a series of overlapped UAV stereo photographic images and shows the landslide scarps of the two landslides in plan view. These scarps define the boundaries of the two landslide episodes and are denoted by solid-coloured lines (red: the first landslide; pink: the second landslide). The scarps of the first and second landslides are both sub-vertical, striking northeast-southwest and approximately north–south, respectively. The rear and lateral release surfaces for the two landslide events are associated with J2/F2 and J4/F4 orientations.

Open tension cracks can be observed on slope surfaces (Fig. 6) as well as behind the crest of the slope. The cracks, developed on and behind the crest of the slope, show some regularity in orientation and appear to begin and propagate along pre-existing discontinuities. Specifically, tilted cracks T1 (Fig. 6b) dipping out the slope may be related to discontinuity set J1 (34°/320°). The sub-vertical cracks T2 are likely to be associated with discontinuity J2 (87°/336°).

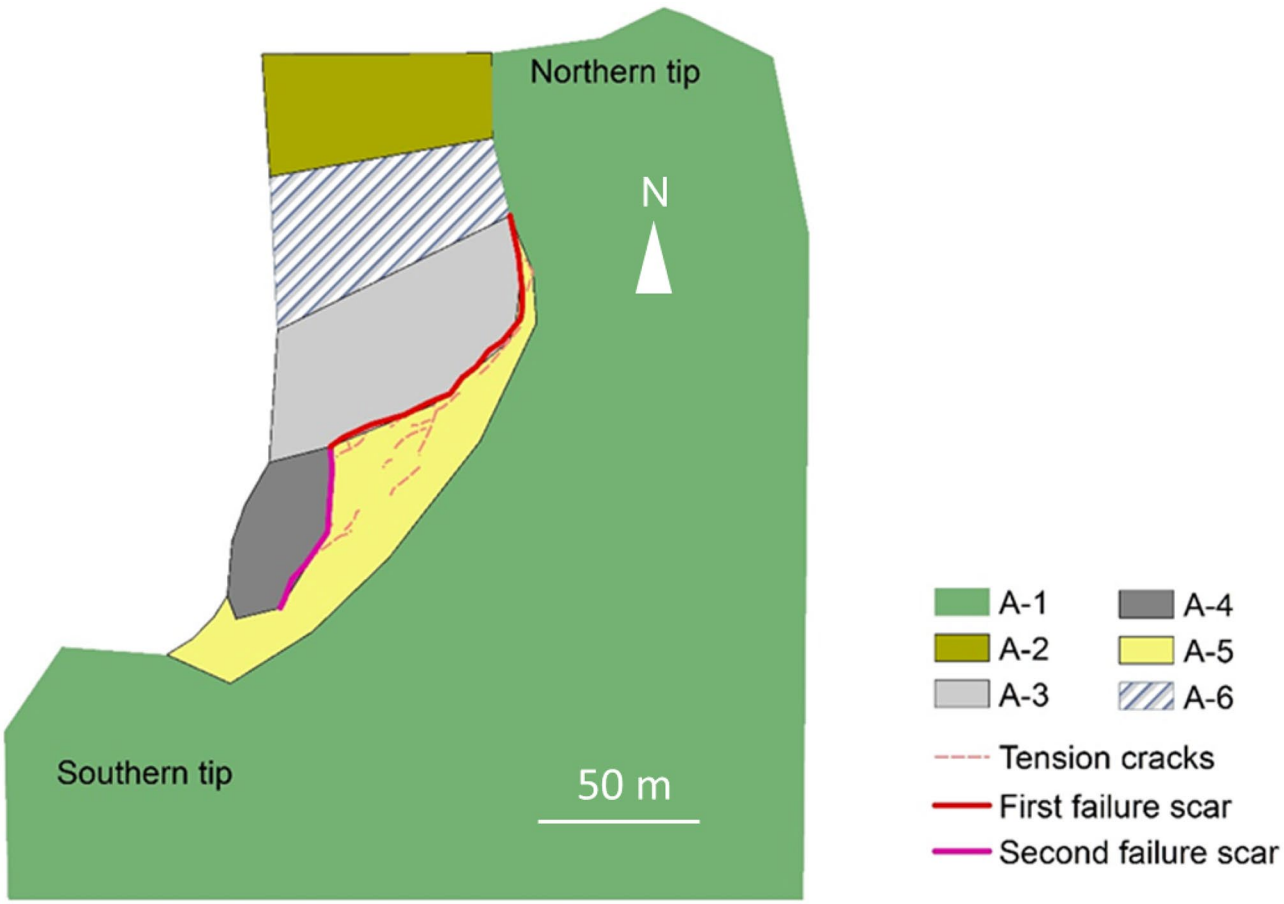

Fig. 7 Plan view showing subdivision of the slope into six zones, including A-1 for currently stable area, A-2 for the triangular rock prism, A-3 for the first landslide area, A-4 for the second landslide area, A-5 for the currently unstable area and A-6 for the inlet

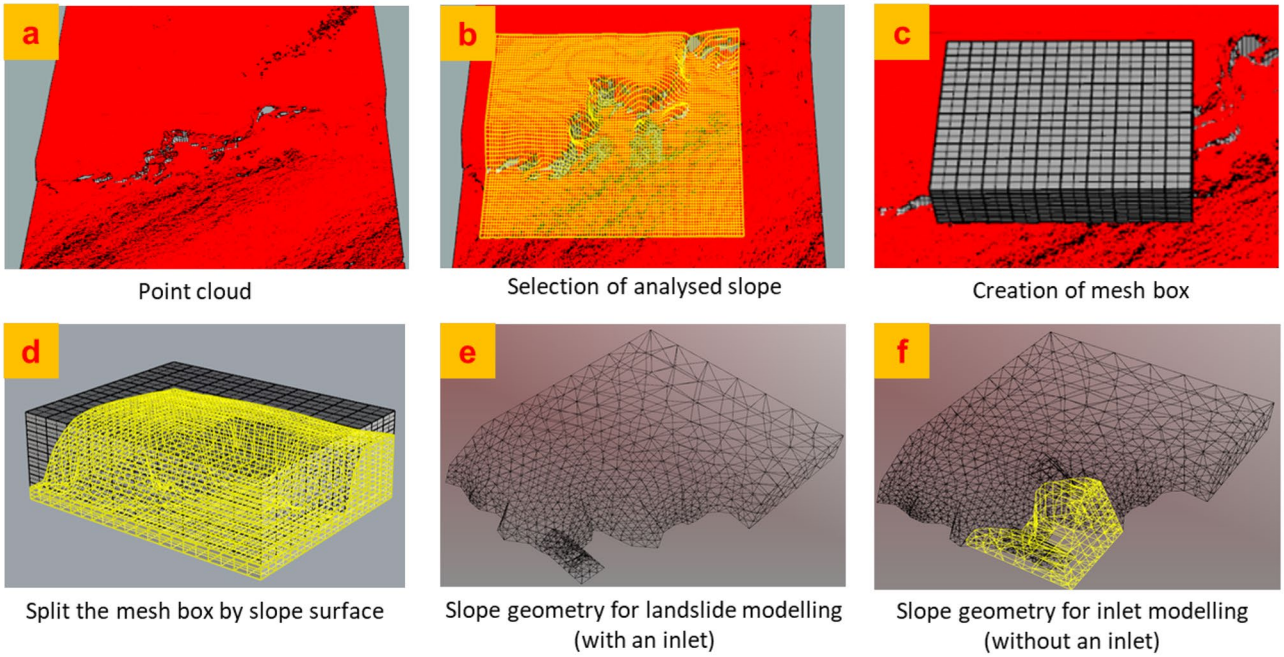

Fig. 8 Construction of three-dimensional models of analysed slope at Hell's Mouth using Rhino software based on 2008 LiDAR point cloud data from A to F: **a**) the point cloud of the coast in year 2008, **b**) the selection of the analysed slope, **c**) creation of a mesh box covering the extent of the slope, **d**) splitting the meshed slope model from the entire coast, **e**) the model for the simulation of two episodes of the Hell's Mouth landslide and **f**) the model for the simulation of inlet formation

Northeast-southwest striking cracks T3 that dip into the slope appear to be developed along discontinuity set J3 (64°/143°). Sub-vertical and north–south striking cracks T4 (Fig. 6c) are related to set J4 (87°/69°).

Slope zone subdivision

The RS survey was used to subdivide the slope into six zones (Fig. 7) for modelling purposes. Zone A-1 represents currently stable areas, covering most of the slope; zone A-2 represents the triangular rock prism forming the cliff geometry on the northern side of the inlet; the first landslide occurred in zone A-3; the second landslide occurred in zone A-4; zone A-5 represents the currently unstable blocks in which tension cracks are detected and zone A-6 forms the region associated with the formation of the inlet. The formation of the inlet provides the kinematic freedom for the first landslide episode in zone A-3. Instability associated with zones A-3 and A-4 results in tension crack development in zone A-5.

Numerical modelling

To analyse the slope instability of a jointed rock mass, a 3D DEM method assuming elastic-perfectly plastic joints was used for the modelling. Validation of the model was undertaken comparing the modelling results (e.g. tension cracks, landslide scars and rock mass damage) with corresponding observations from field surveys.

Model geometry and properties

The construction of two models

Three-dimensional models that consist of discrete and interconnected triangular meshes were constructed for the numerical modelling analysis by using Rhino software (Robert McNeel and Associates 2012). The construction process for the models is presented as follows.

Table 2 Properties of discontinuities applied in 3DEC modelling, including geometry parameters (spacing and persistence) and deformation/strength parameters (normal stiffness, shear stiffness, friction angle and cohesion)

Discontinuity		Spacing (m)	Persistence (%)	Normal stiffness (MPa/m)	Shear stiffness (MPa/m)	Friction angle (°)	Cohesion (MPa)
Joint sets	S0	5	80	100	10	30	1/0
	J1		50			32	
	J2		80			30	
	J3					32	
	J4					30	
Faults	F2	(None)	100			20	0
	F3						

1) As shown in Fig. 8a, a point cloud (year 2008) was acquired from the open-source Channel Coastal Observatory (CCO) (Channel Coastal Observatory 2020) to provide the slope geometry after the inlet formation and prior to the Hell's Mouth landslide.
2) Fig. 8b–d show the construction of a 3D meshed model from a point cloud. Figure 8e presents the geometry of the modelled slope formed before the occurrence of the Hell's Mouth landslide and after the formation of the inlet for the numerical analysis of two landslide episodes.
3) In order to assess the evolution of the inlet and its influence on proximal slope stability, a second model was constructed. This was performed by manually plotting the complementary section in zone A-6 (Fig. 8f), to represent the slope prior to inlet formation.

The two generated models (Fig. 8e and f) are defined by a global Cartesian coordinate system, where the X axis refers to the east, Y axis indicates the north direction and Z axis coincides with the vertical direction. A fixed boundary condition was applied to the base, east wall, west wall and south wall of the model, whilst the north surface was kinematically free to allow simulation of landsliding. Boundaries were extended from the zone of interest to ensure no boundary effects (model was 250 m * 270 m * 70 m). During the modelling, any detached blocks could freely drop so as not to allow accumulation at the base of the slope (to simulate the removal of blocks by wave action).

Two observed sub-vertical faults (F2 and F3), shown in Fig. 3, were plotted crossing through the model to act as release surfaces constraining the geometry of the inlet. In addition, five previously identified discontinuity sets were also created in the model with their retrospective orientations, spacing and persistence (see Table 2).

Model setting

As previously indicated, the 3D DEM code 3DEC (Itasca Consulting Group Inc. 2017) was used for numerical analysis. The code uses an explicit time-stepping system to solve equations of motion, simulating the response of rock mass that is subject to either static or dynamic loading (Itasca Consulting Group Inc. 2017). Individual blocks can behave as rigid or deformable, depending on specific situations. In this paper, rigid blocks were assumed as the analysed slope is representative of a relatively stiff rock mass. The joint constitutive model used for the modelling adopted elastic–plastic contact mechanics through the Mohr–Coulomb slip failure criterion.

Table 3 Variations in dip, dip direction, persistence and friction angle of J1 set that were characterised by mean, minimum and maximum values

J1 property	Mean value	Minimum	Maximum
Dip (°)	34	24	44
Dip direction (°)	320	300	340
Persistence (%)	50	30	70
Friction angle (°)	32	22	42

During application of in situ stresses in the slope, the model was brought to initial equilibrium by applying high friction angle values to discontinuities. Under these conditions, the in situ vertical stress at each point can be calculated from the weight of overlying material. The horizontal stresses were proportional to that of the vertical. The mechanical behaviour of the slope was simulated following equilibrium by reducing the discontinuity friction angle to the values provided in Table 2. An adaptive global damping strategy was applied at the first stage so that the model was able to reach a force equilibrium state as quickly as possible, by adjusting the viscosity such that the power absorbed by damping is a constant proportion of the rate of change of kinetic energy in the system (Hart et al. 1988). However, global damping was not considered appropriate for all localised case studies associated with DEM modelling to solve static solutions (Itasca Consulting Group Inc. 2017). Therefore, a local damping mode was adopted after the model was brought to equilibrium for the slope failure analysis.

Table 2 provides discontinuity properties assumed for the model. Where possible, field data was used to determine the material parameters. This was supported with data from related

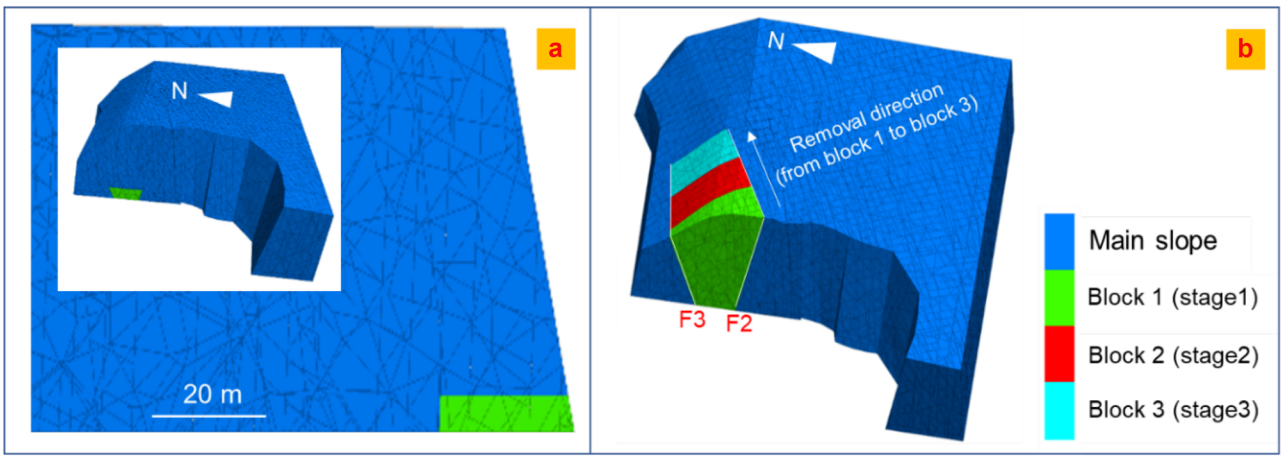

Fig. 9 Different strategies for modelling the inlet formation: **a**) method 1 for investigating the effect of toe erosion on the stability of overlying rock blocks, **b**) method 2 for investigating the effect of sequential removal of inlet blocks on the stability of adjacent zones

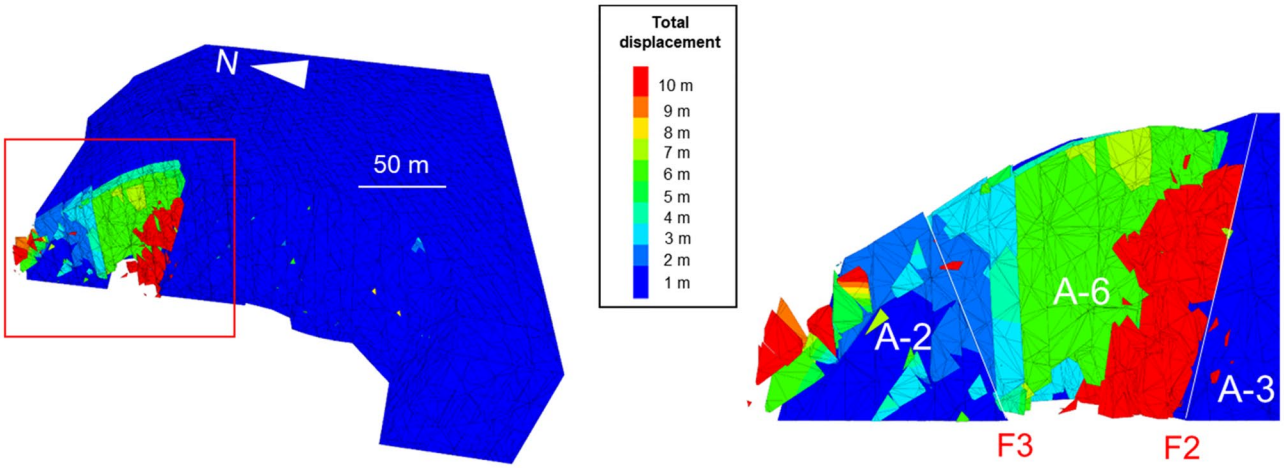

Fig. 10 Results of modelling method 1, showing total displacements developed in the vicinity of the inlet caused by wave erosion

publications and previous work (Hobbs et al. 2002; Vanneschi et al. 2019). Note that persistence used in 3DEC refers the probability that any given block lying in the path of a joint will be split on average (i.e. if persistence = 50%, then 50% of the blocks will be split) (Itasca Consulting Group Inc. 2017). Lower shear strength and material properties were assigned to the faults, compared with joints, i.e. lower cohesion and friction angle values. A higher value of cohesion was assumed for J1 during inlet formation to ensure the representative cliff geometry was established prior to modelling of the landslide. A reduced cohesion (0 MPa) was used to simulate strength deterioration potentially caused by weathering (Martin et al. 2011; Mousavi et al. 2019), rock bridge failure (Kemeny 2003) and time-dependent deterioration (Aydan et al. 2012).

Model simulations

Inlet formation

The model shown in Fig. 8f was used for modelling the inlet formation. To simulate the impact of block removal through toe erosion on the inlet formation and investigate the influence of the progressive development of the inlet on adjacent slope stability, two modelling strategies were implemented.

1) Method 1: toe erosion characterised by the removal of rock blocks at the toe of the slope was carried out to investigate its effect on the stability of overlying rock mass. The sequence of the toe removal is presented in Fig. 9a.
2) Method 2: a simplified progression of the inlet, as shown in Fig. 9b, was conducted to investigate its influence on the proximal slope stability. In the modelling, the gradual progressive formation of the inlet was simulated by sequential removal of rock blocks 1, 2 and 3, respectively.

Landslide development and tension crack formation

The formation of the inlet provided daylighting conditions for discontinuities exposed on the inlet sidewalls. A three-dimensional model generated from LiDAR point cloud data (year 2008) was applied (as shown in Fig. 8e) to restore the pre-landslide geometry of the slope. The two 2011 failure episodes were then modelled in a single simulation. The modelling results were then compared with observations of tension crack formation and scar location/extent resulting from the two failures. These observations were taken from

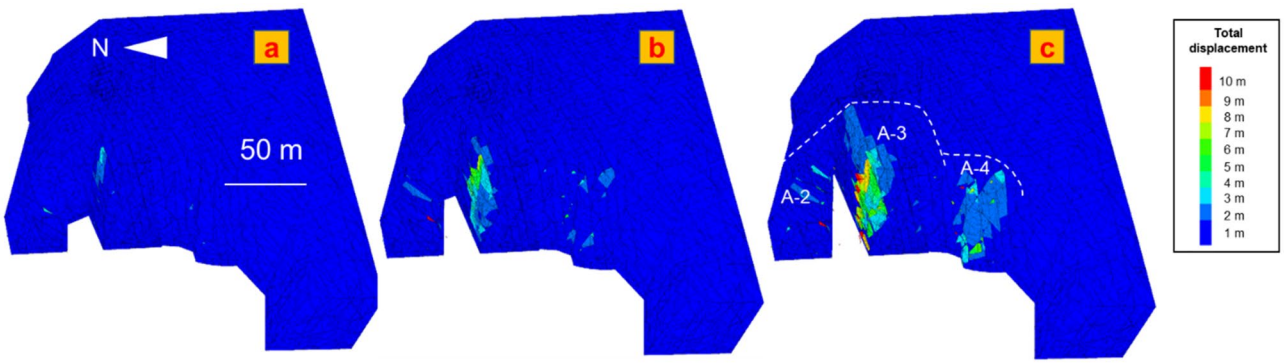

Fig. 11 Results of modelling method 2, showing total displacements of blocks occurred in the three model stages: **a**) stage 1; **b**) stage 2; **c**) stage 3

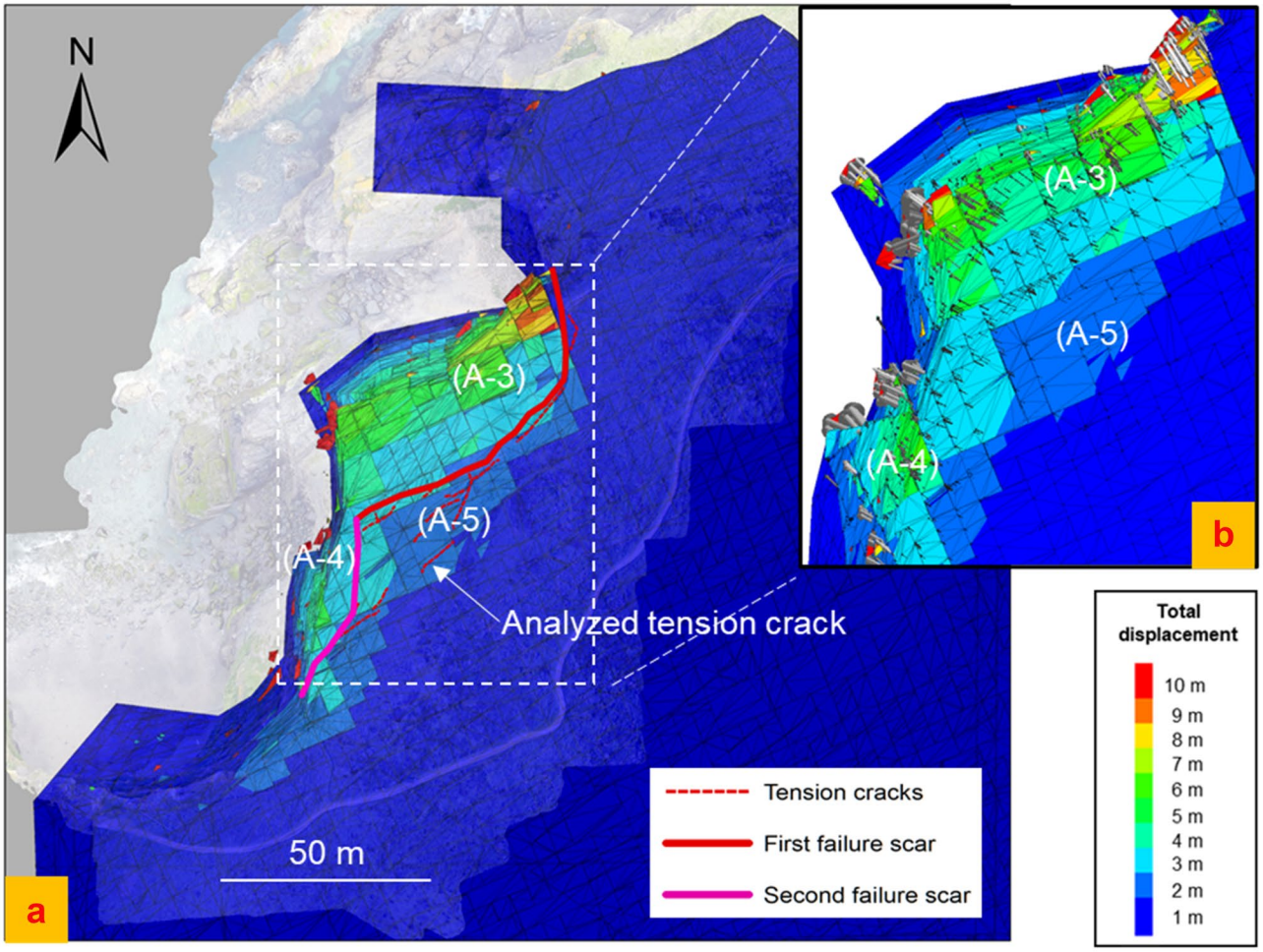

Fig. 12 3DEC modelling results: a) plan view showing comparison of modelled total displacement contours with field observations of landslide scars and tension crack development behind the crest of the cliff; b) plan view of modelled total displacement contours with displacement vectors included.

remote sensing survey data and aerial photographs of the site location. Cross-sections through the 3DEC model were taken to monitor the modelled tension crack development, providing a comparison between the simulated tension cracks and the observed tension cracks behind the cliff with respect to their orientations and locations. The model results were then used to investigate the failure mechanism of the two landslides through the evaluation of cross-sections taken through the 3DEC model in different directions.

In addition, further insight into the potential opening of a modelled tension crack developed upon a J3 plane (64°/143°) is provided by using the differential displacement analysis of two adjoining rock blocks. The displacements of two blocks in the X, Y, Z direction provides a basis to analyse the movement directions of the blocks, characterised by mean plunge and azimuth of block displacements in the model every 1000 calculation timesteps.

Sensitivity analysis

Francioni et al. (2018a) identified five discontinuity sets within the rock mass which exhibit data dispersion of orientations (Fig. 2a). A sensitivity analysis was carried out to assess the potential impact of variations in orientation of key discontinuities on slope behaviour. Considering that the two landslide episodes were principally controlled by J1 (Francioni et al. 2018a), this was selected as the critical discontinuity for further sensitivity analysis.

The sensitivity analysis concentrated on dip, dip direction, persistence and friction angle of joint set J1. Variations in these parameters were characterised by mean value, minimum and maximum, as shown in Table 3. A series of models were undertaken using a control variate method by which each discontinuity parameter is individually and sequentially varied (Vanneschi et al. 2019), to investigate the effects of variation of each parameter alone by the comparison of the related modelling results. For each analysed parameter, a sensitivity analysis was conducted by varying its value from the minimum, the mean, to the maximum and analysing the effect of this change.

Results

Simulation of toe erosion and inlet formation

With respect to modelling method 1, for investigating the influence of block removal and potential wave erosion, the results

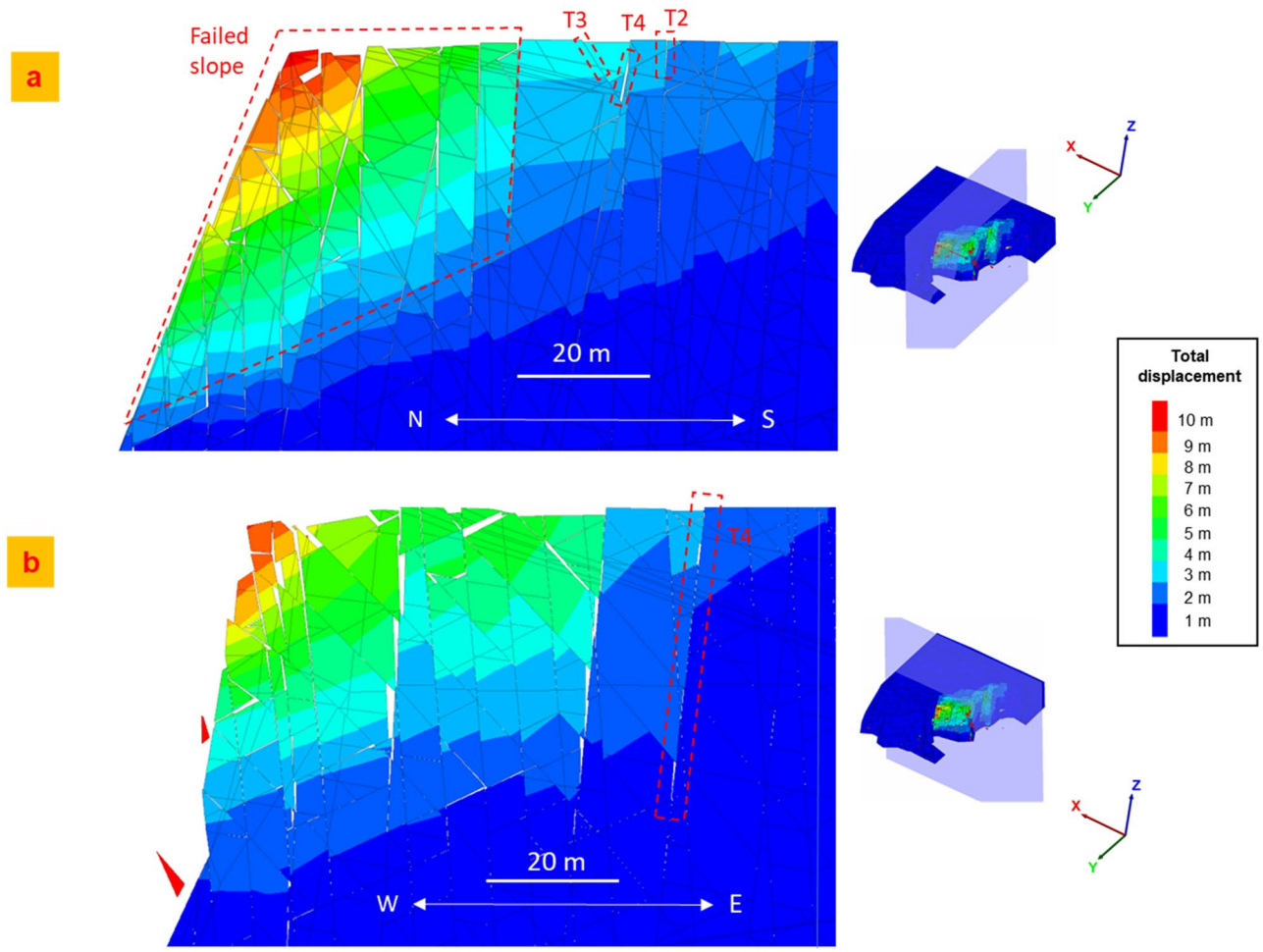

Fig. 13 Cross-sections of 3DEC analysis for the region of the first landslide episode showing the total displacement of blocks: **a**) north–south, **b**) east–west

presented in Fig. 10 show that toe removal causes the collapse of overlying blocks. This is constrained by the F2, F3 and joints in set J4, which act as lateral (F2 and F3) and rear (J4) release surfaces, respectively. In addition, minor planar failures are observed in the proximity of the inlet in zone A-2, sliding along J1 planes resulting from kinematic release associated with the newly formed inlet face and daylighting features.

Regarding modelling method 2, for understanding influences of the progressive inlet formation on proximal slopes, the results presented in Fig. 11 indicate that the removal of the three blocks leads to progressive displacement of the proximal blocks in zone A-3, directly adjacent to the inlet sidewalls. Displacements within the southern inlet sidewall are greater at the western edge of the inlet than those simulated at the eastern edge. This reflects the sequence of block removal and progressive formation of the inlet. In addition, minor displacements were also detected in the scarp of zone A-4, as well as in the southern scarp of zone A-2.

Simulation of the two landslides

The results for the modelled landslides at timestep 5000 are presented in Fig. 12 and highlight two regions of increased deformation for both the northern and western faces of the cliff. Major displacements occur within zones A-3 and A-4 (representing the two landslide episodes) with minor displacements in zone A-5 (the region of current tension crack development). The scars for both landslide events and the observed field tension crack development are superimposed on the modelling results shown in Fig. 12a. A good agreement can be observed between the modelled results and field observations. Vectors of block resultant displacement are presented in Fig. 12b, which confirms that displacements in zones A-3 and A-4 are greater than that in zone A-5, with all three regions showing a general displacement trend towards the northwest.

In order to provide further understanding of the modelled block interaction and landslide development, cross-sections were taken through the 3DEC model in different directions. For the first

landslide location, a north–south and an east–west cutting plane were created, as depicted in Fig. 13. This shows the total displacement of blocks along the selected cross-sections. Figure 13a provides a north–south cross-section that highlights the controlling influence of discontinuity set J1 which dips out of the face and forms a potential basal sliding plane. Increased deformation towards the top of the cross-section suggests the potential influence of toppling which is controlled by the aspect ratio of rock columns formed by discontinuity sets J2, J3 and J4. Figure 13b provides an east–west cross-section and shows the development of an active–passive wedge at the base of the slope and further potential for toppling. These observations support the findings from the video-frame analysis described in the 'Previous landsliding activities' section. The video was taken from the adjacent cliff looking towards north-east, so Figs. 13b and 14a provide the closest matching views. Both Fig. 13a and b show potential tension crack opening behind the modelled slope crest, with the specific discontinuity orientations highlighted. Note the label 'T' is used to depict a tension crack formed from a particular discontinuity orientation (i.e. T1 associated with J1 etc.).

Figure 12 shows cross-sections taken through the 3DEC model in the area of the second landslide. Again, the influence of potential basal features and toppling can be observed, particularly in Fig. 14a, where the active–passive wedge and toppling observed in the video-frame analysis is replicated.

Opening of tension cracks

The opening of internal joints within the model slope has been investigated, by identifying joint opening on the north–south cross-section shown in Fig. 13a for different calculation timesteps using the software Fiji (ImageJ based) (Schindelin et al. 2012). It can be seen from Fig. 15 that opening of joints in the unstable zone (A-5) is less noticeable than that in the failure zone (A-3), which is more obvious in Fig. 15c and d. The analysis allows quantification of opening of modelled joints.

A north–south cross-section (presented in Figs. 12a, 13a, 15d) of the tension crack, T3, have been recorded at steps 6000, 11,000 and 14,000 to provide the visualisation of the tension crack development (Fig. 16). In Fig. 16, ground depression is observed with relatively lowering of block 2.

The lowering of blocks behind the crest of the cliff is also observed in the field, as shown in Fig. 17, which shows recent photographs taken of the region of tension cracks formed behind the crest of the cliff section.

In order to analyse movement of the modelled joints or cracks, T3 is used to record the displacements of the two adjoining rock blocks. A differential displacement behaviour in X, Y, Z directions can be observed between blocks 1 and 2. Specifically, during the development of the joint-controlled tension crack, T3, block 1 is displaced preceding block 2 in X and Y directions with gradually

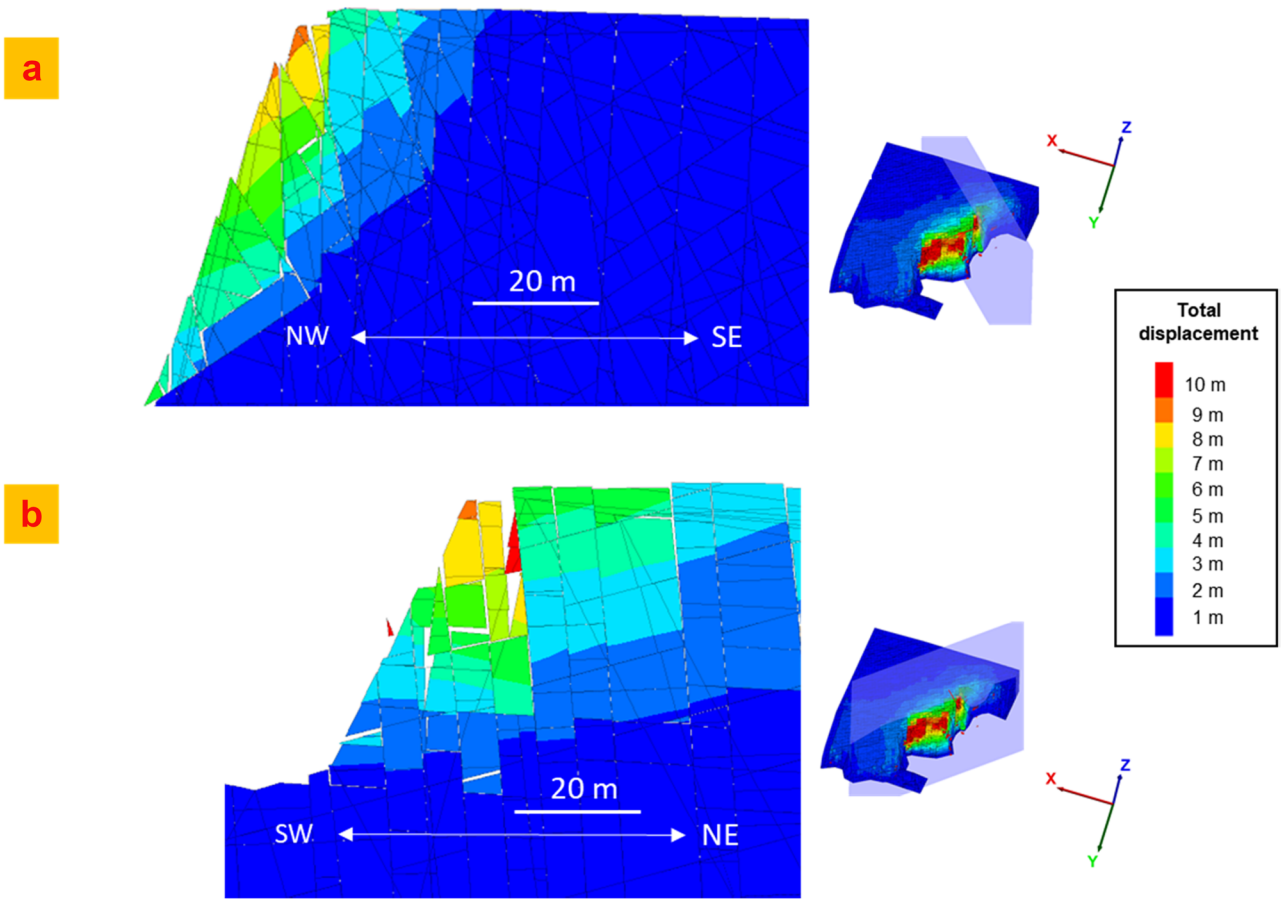

Fig. 14 Cross-sections of 3DEC analysis for the region of the second landslide episode showing the total displacement of blocks: **a**) north-west-southeast, **b**) northeast-southwest

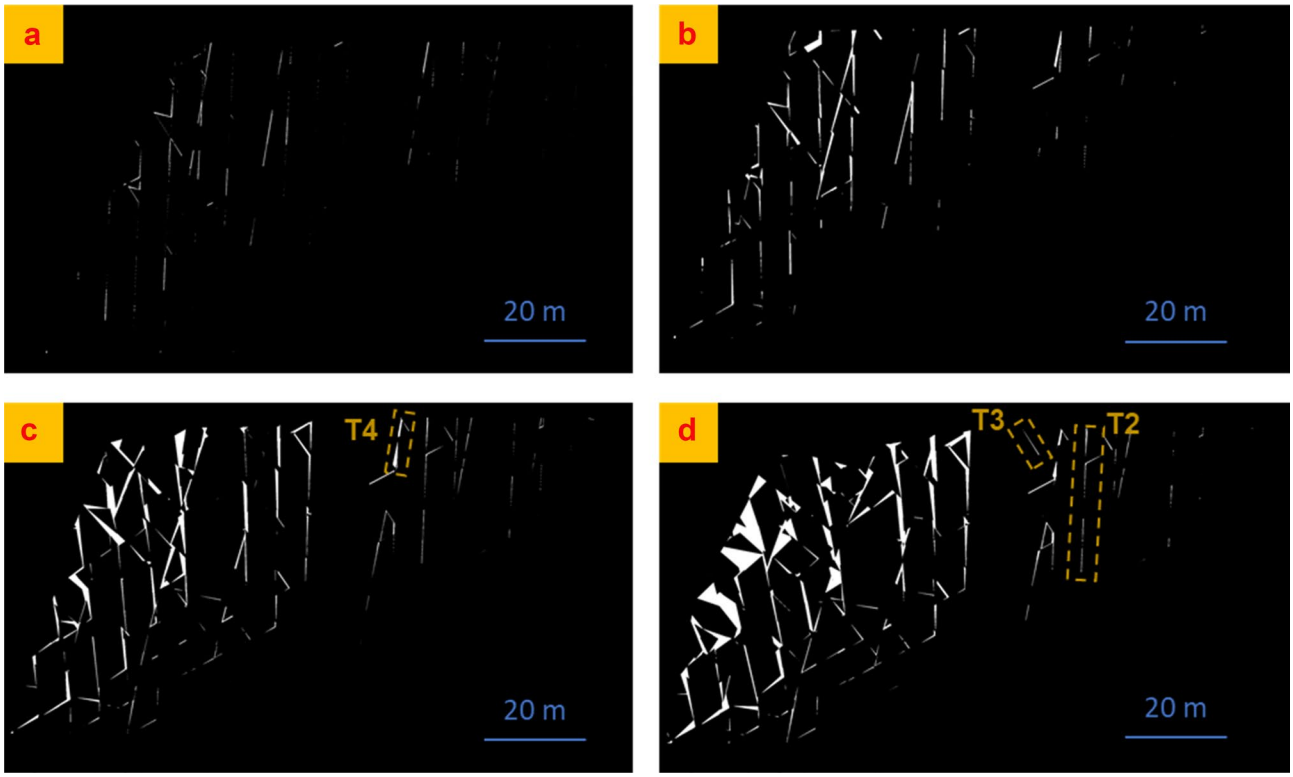

Fig. 15 Identified joint opening (voids and joint-cracks) on the north–south cross-section (shown in Fig. 13a) at different timesteps, **a**) timestep 1000, **b**) timestep 5000, **c**) timestep 9000, **d**) timestep 13,000

increased opening (Fig. 18a and b). However, with respect to the Z direction, more displacement of block 2 is observed (Fig. 18c).

Displacement directions of the two blocks can be assessed by mean plunge angles and azimuth angles for every 1000 calculation timesteps (Fig. 19). The azimuth curves fluctuate between 270 and 310° (Fig. 19a), lower than the landslide sliding direction (320°) controlled by J1, as well as the toppling direction (323°) controlled by J3 (as indicated in Fig. 2). In general, the plunge of block 2 is greater than that of block 1, resulting from significantly more Z direction displacement (Fig. 19b). The plunge of block 2 is zero at step 14,000, as a result of no displacement of block 2 in the Z direction at that time.

Sensitivity analysis for J1

Figure 20 shows the influence of variation in the dip of J1 on the modelled results in plan view. When the dip of J1 is reduced to 24° from its original value (34°), less displacement and reduced extent of slope deformation are observed. As expected, greater deformation and a larger region of instability are formed when the dip of J1 is increased to 44°.

The results shown in Fig. 21 clearly show the influence of dip direction of J1 on the slope stability. When the dip direction is reduced to 300°, modelling shows that west-dipping slopes in zones A-2 and A-3 are more prone to failure, whereas an increase in the

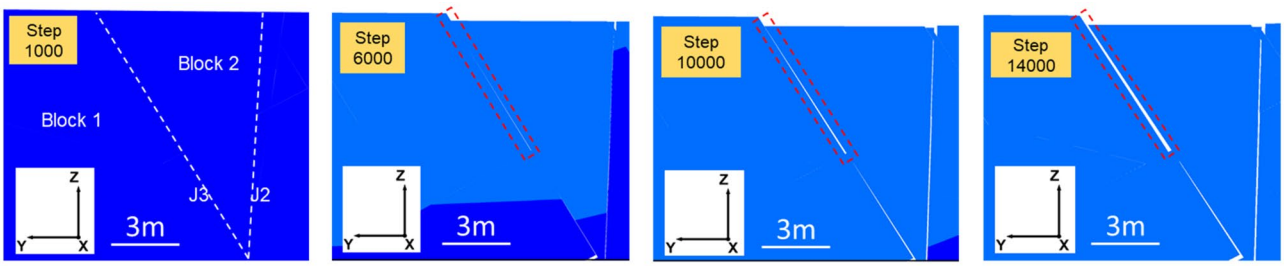

Fig. 16 North–south cross-sections through the 3DEC model at different calculation timesteps, showing the development of a tension crack associated with opening along a J3 plane and relatively lowering of the block 2

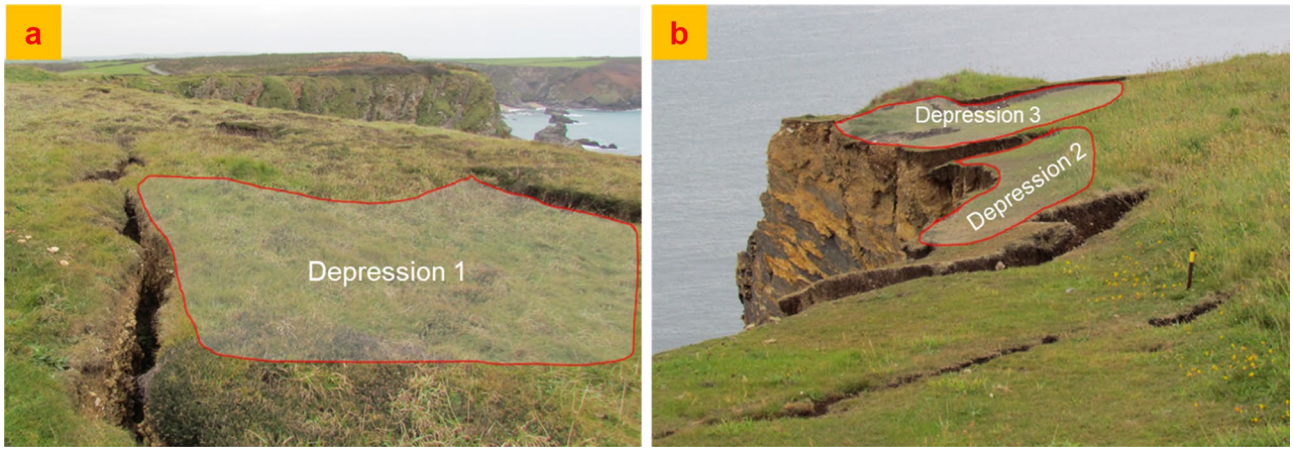

Fig. 17 Depressions occurred along with the opening of tension cracks in the unstable slope. **a**) An image looking towards west, **b**) an image looking towards north

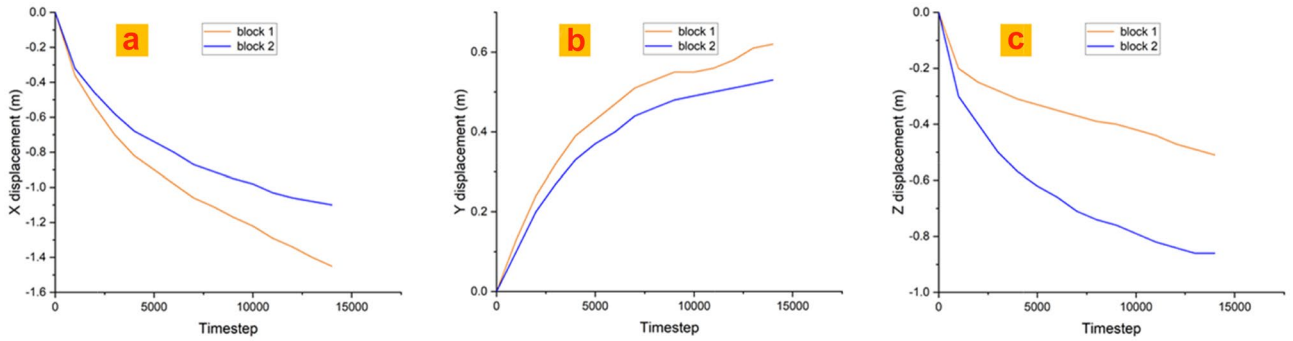

Fig. 18 Displacement curves of block 1 (orange lines) and 2 (blue lines): **a**) block displacements in X direction, **b**) block displacements in Y direction, **c**) block displacements in Z direction

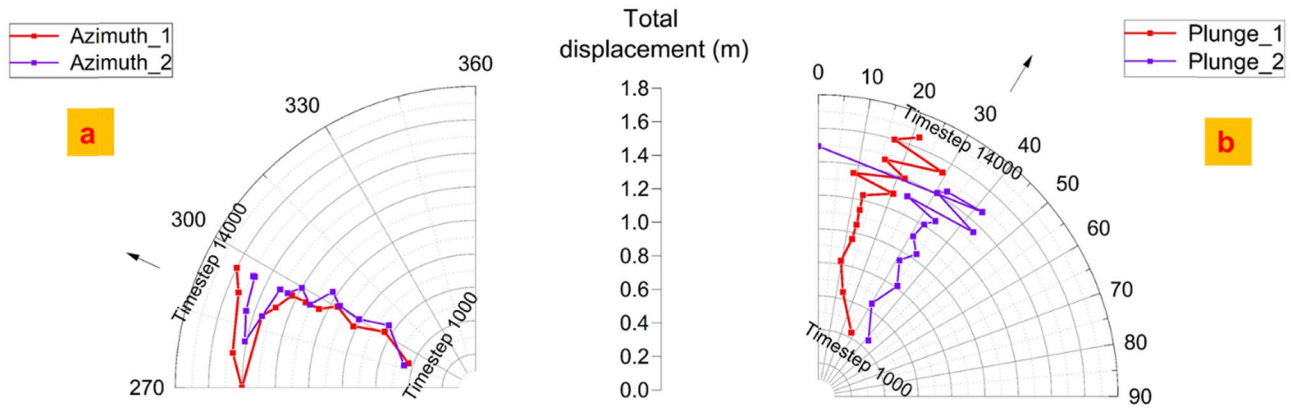

Fig. 19 Hodographs of mean movement directions of the two blocks with block total displacement in each 1000 timesteps: **a**) the azimuth of the trajectory; **b**) the plunge of the trajectory

dip direction causes more potential for north-dipping slopes, particularly at the eastern tip of the inlet to become unstable. This is also reflected in stereonet plots that when the dip direction of J1 varies from 300 to 340°, the displacement directions of potential instabilities, caused by J1 set or its interaction with other sets, generally change from west to a more northerly direction (as depicted in Fig. 22).

The effect of persistence is presented in Fig. 23. This indicates that the persistence has a critical influence on the extent of potential instability. An increase in discontinuity persistence from 30 to 70%

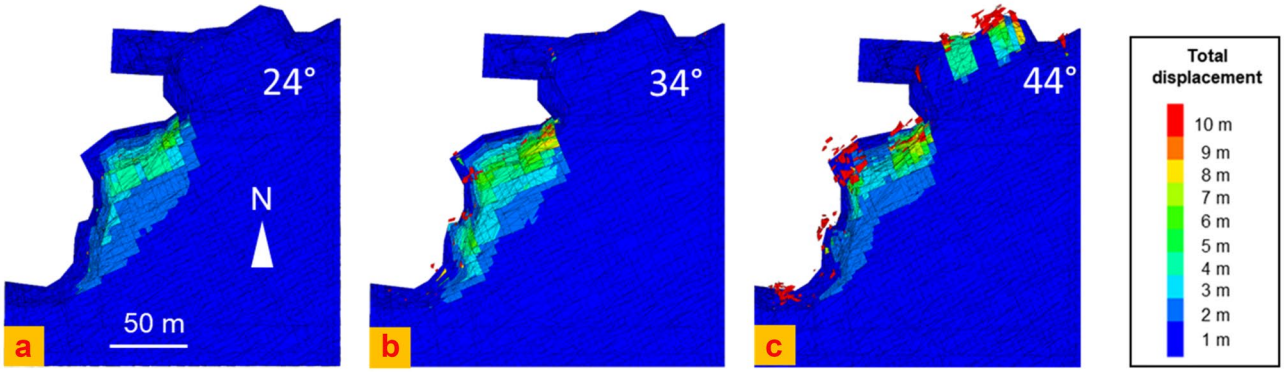

Fig. 20 Sensitivity analysis of J1 dip angle by varying from 24 to 44° in plan view, **a**) 24°, **b**) 34° and **c**) 44°

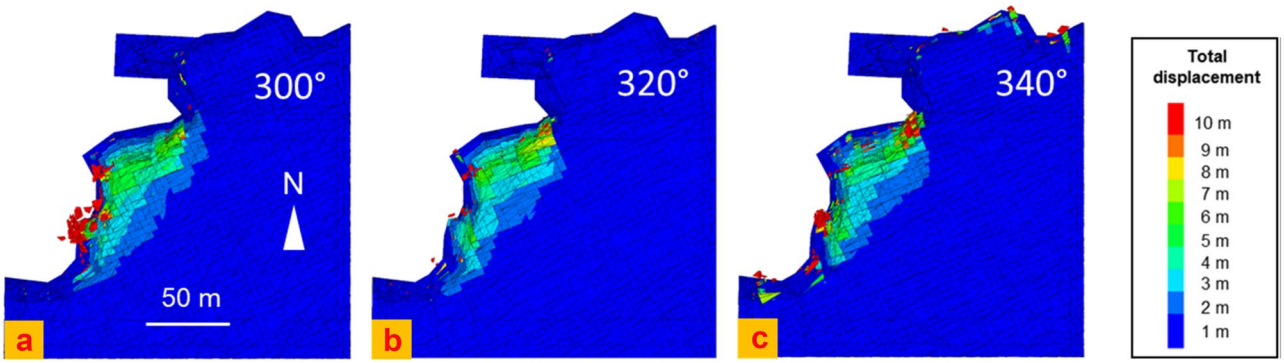

Fig. 21 Sensitivity analysis of J1 dip direction by varying from 300 to 340° in plan view, **a**) 300°, **b**) 320° and **c**) 340°

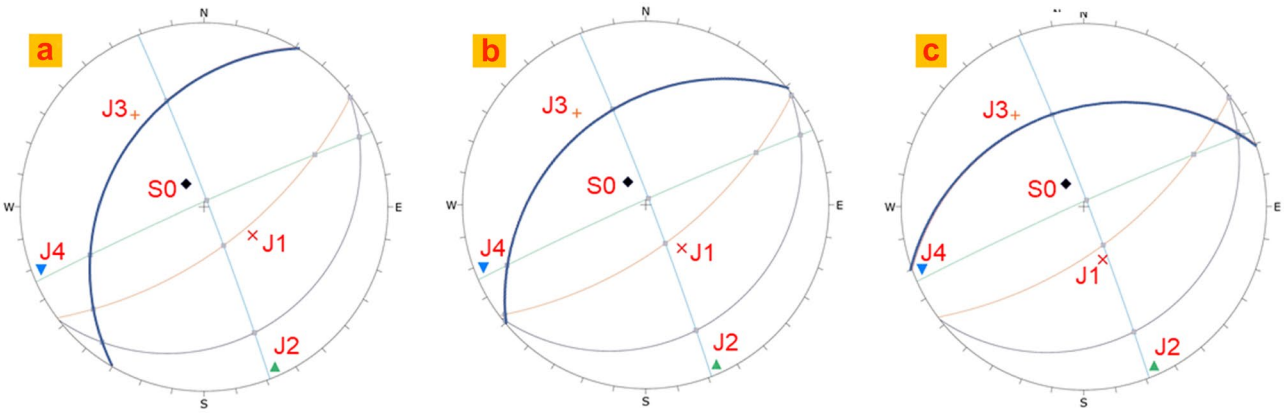

Fig. 22 Stereonet plots showing orientations of joint sets and intersections with variations in J1 dip direction from **a**) 300°, **b**) 320° and **c**) 340°

results in the enlargement of the failed zone, particularly at the eastern end of the north-dipping slope and more deformation/influence in the region of the second landslide event on the west-dipping slope.

When evaluating the influence of modelled friction angle, the extent of the first and second landslides appears not to be significantly influenced by variations of friction angle. However, as would be expected, when the friction angle is decreased from 32 to 22°, the total displacement of the unstable rock blocks rises, which is shown in Fig. 24.

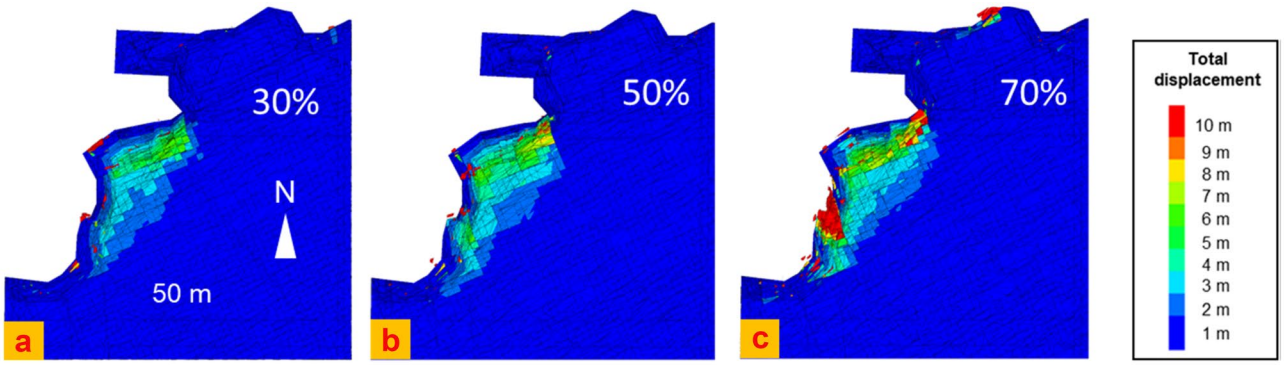

Fig. 23 Sensitivity analysis of J1 persistence by varying from 30 to 70% in plan view, **a**) 30%, **b**) 50% and **c**) 70%

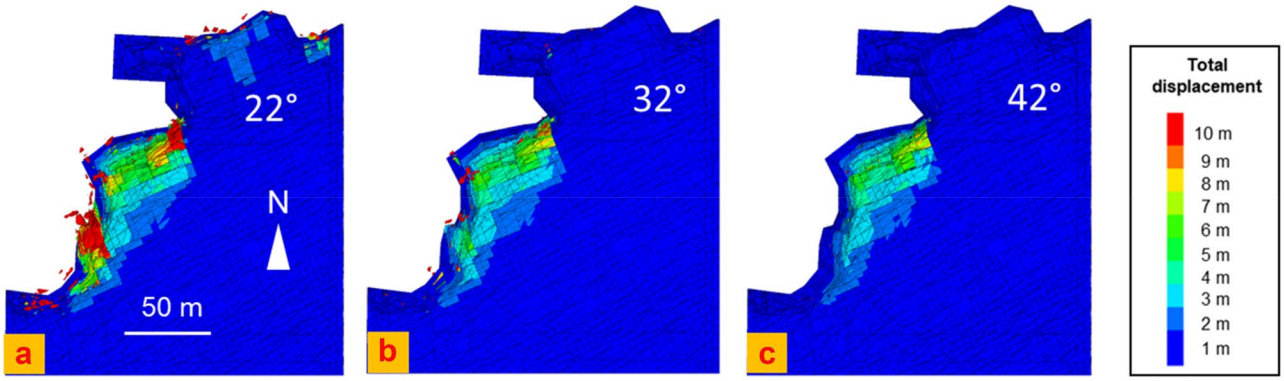

Fig. 24 Sensitivity analysis of J1 friction angle by varying from 22 to 42° in plan view, **a**) 22°, **b**) 32° and **c**) 42°

Discussion and conclusion

This paper presents the results of a back analysis of a landslide that occurred at Hell's Mouth on the north coast of Cornwall, to provide further understanding of the coastal cliff erosion processes and the kinematics of the slope failure mechanisms involved. The landslide occurred as two separate events over a 3-month period. In view of the discontinuity-controlled nature of the failures, 3DEC modelling was undertaken. Modelling included the evolution and formation of an inlet, and the influence of discontinuities on potential landslide failure mechanisms and tension crack development behind the crest of the slope. A video recording of the initial failure was used to constrain the interpretation of the modelled results. Due to potential variations of discontinuity properties associated with the potential basal plane associated with planar sliding, wedge sliding and topping failure, a series of sensitivity analyses were undertaken to investigate the effects of these uncertainties on slope stability analysis. The key conclusions arising from the study are:

1) The simulation of inlet formation shows that block removal (from wave erosion) would result in sequential instability of overlying blocks restricted or confined by two sub-vertical faults, consequently forming the inlet. During progressive inlet formation, modelling shows the potential for daylighting features in the newly exposed inlet sides to form, resulting in potential for discontinuity-related instability from the southern inlet sidewall.
2) Numerical modelling of the landslide events highlights the controlling influence of the potential basal feature (J1), which is also influenced by lateral release surfaces associated with J2 and rear release surfaces associated with J4. J3 may also contribute to toppling failures.
3) The sequence of events captured in the video taken during the initial failure is effectively reproduced by the 3DEC model. This includes the development of an active–passive wedge near the base of the slope, together with evidence of wedge and toppling failure.
4) 3DEC modelling was also able to effectively capture the opening of tension cracks on pre-existing discontinuities behind the crest of the slope. Modelled tension crack formation was detected behind the crest of the landslide zones. Cross-sections taken through the 3DEC model strongly suggests that the observed tension cracks formed along pre-existing discontinuities. The tension cracks appear to be primarily associated with more steeply inclined discontinuities (J2, J3, J4) with visible daylighting on the slope surface.
5) Sensitivity analysis highlighted the importance of fracture network orientations relative to slope geometry on potential landslide failure mechanisms with respect to the size and spatial distribution. The sensitivity analysis also highlighted the effect of dip, dip direction and persistence of the basal feature on the extent and spatial distribution of potential slope instability.

6) Use of a hodographic interpretation of block displacements in association with stereographs can aid in interpreting complex rock slope failure mechanisms with a 3DEC-DFN model.

Acknowledgements

First and foremost, we would like to express our sincere gratitude to Digimap for providing access to geological data. Secondly, we would like to thank the British Geological Survey (BGS) for access to records of historic UK coastal landslides.

Author contribution

Conceptualisation: John Coggan, Lingfeng He, Matthew Eyre; methodology: John Coggan, Lingfeng He, Matthew Eyre, Doug Stead, Mirko Francioni; formal analysis and investigation: Lingfeng He, Matthew Eyre, Mirko Francioni; writing—original draft preparation: Lingfeng He; writing—review and editing: Lingfeng He, John Coggan, Doug Stead, Matthew Eyre, Mirko Francioni.

Availability of data and material

Not applicable.

Code availability

Not applicable.

Declarations

Ethics approval Not applicable.

Consent to participate Not applicable.

Consent for publication Not applicable.

Conflict of interest The authors declare no competing interests.

References

Agisoft (2016) Metashape. Agisoft LLC

Agliardi F, Riva F, Barbarano M, Zanchetta S, Scotti R, Zanchi A (2019) Effects of tectonic structures and long-term seismicity on paraglacial giant slope deformations: Piz Dora (Switzerland). Eng Geol 263:105353. https://doi.org/10.1016/j.enggeo.2019.105353

Aydan Ö, Uehara F, Kawamoto T (2012) Numerical study of the long-term performance of an underground powerhouse subjected to varying initial stress states, cyclic water heads, and temperature variations. Int J Geomech 12:14–26. https://doi.org/10.1061/(ASCE)GM.1943-5622.0000040

Bovis MJ, Evans SG (1996) Extensive deformations of rock slopes in southern Coast Mountains, southwest British Columbia. Canada Eng Geol 44:163–182. https://doi.org/10.1016/S0013-7952(96)00068-3

Brideau MA, Pedrazzini A, Stead D, Froese C, Jaboyedoff M, van Zeyl D (2011) Three-dimensional slope stability analysis of South Peak, Crowsnest Pass, Alberta, Canada. Landslides 8:139–158. https://doi.org/10.1007/s10346-010-0242-8

Brideau MA, Stead D, Roots C, Orwin J (2007) Geomorphology and engineering geology of a landslide in ultramafic rocks, Dawson City. Yukon Eng Geol 89:171–194. https://doi.org/10.1016/j.enggeo.2006.10.004

British Geological Survey (2020) Hell's Mouth, Cornwall - landslide case study. Br. Geol. Surv. https://www.bgs.ac.uk/case-studies/hells-mouth-cornwall-landslide-case-study/. Accessed 22 Feb 2021

Channel Coastal Observatory (2020) Channel Coastal Observatory. https://www.channelcoast.org/

Corkum AG, Martin CD (2004) Analysis of a rock slide stabilized with a toe-berm: a case study in British Columbia, Canada. Int J Rock Mech Min Sci 41:1109–1121. https://doi.org/10.1016/j.ijrmms.2004.04.008

Digimap (2020) Digimap. https://digimap.edina.ac.uk/lidar

Donati D, Stead D, Brideau MA, Ghirotti M (2021a) Using pre-failure and post-failure remote sensing data to constrain the three-dimensional numerical model of a large rock slope failure. Landslides 18:827–847. https://doi.org/10.1007/s10346-020-01552-x

Donati D, Stead D, Elmo D, Borgatti L (2019) A preliminary investigation on the role of brittle fracture in the kinematics of the 2014 San Leo landslide. Geosciences 9:256. https://doi.org/10.3390/geosciences9060256

Donati D, Stead D, Stewart TW, Marsh J (2020) Numerical modelling of slope damage in large, slowly moving rockslides: insights from the Downie Slide, British Columbia. Canada Eng Geol 273:105693. https://doi.org/10.1016/j.enggeo.2020.105693

Donati D, Westin AM, Stead D, Clague JJ, Stewart TW, Lawrence MS, Marsh J (2021b) A reinterpretation of the Downie Slide (British Columbia, Canada) based on slope damage characterization and subsurface data interpretation. Landslides 18:1561–1583. https://doi.org/10.1007/s10346-020-01601-5

Dong M, Kulatilake PHSW, Zhang F (2018) Deformation and stability investigations in 3-D of an excavated rock slope in a hydroelectric power station in China. Comput Geotech 96:132–149. https://doi.org/10.1016/j.compgeo.2017.10.019

Fan W, Lv J, Cao Y, Shen M, Deng L, Wei Y (2019) Characteristics and block kinematics of a fault-related landslide in the Qinba Mountains, western China. Eng Geol 249:162–171. https://doi.org/10.1016/j.enggeo.2018.12.019

Francioni M, Coggan J, Eyre M, Stead D (2018a) A combined field/remote sensing approach for characterizing landslide risk in coastal areas. Int J Appl Earth Obs Geoinformation 67:79–95. https://doi.org/10.1016/j.jag.2017.12.016

Francioni M, Salvini R, Stead D, Coggan J (2018b) Improvements in the integration of remote sensing and rock slope modelling. Nat Hazards 90:975–1004. https://doi.org/10.1007/s11069-017-3116-8

Gao G, Meguid MA, Chouinard LE, Xu C (2020) Insights into the transport and fragmentation characteristics of earthquake-induced rock avalanche: numerical study. Int J Geomech 20:04020157. https://doi.org/10.1061/(ASCE)GM.1943-5622.0001800

Hart R, Cundall PA, Lemos J (1988) Formulation of a three-dimensional distinct element model—part II. Mechanical calculations for motion and interaction of a system composed of many polyhedral blocks. Int J Rock Mech Min Sci Geomech Abstr 25:117–125. https://doi.org/10.1016/0148-9062(88)92294-2

He L, Coggan J, Francioni M, Eyre M (2021) Maximizing impacts of remote sensing surveys in slope stability—a novel method to incorporate discontinuities into machine learning landslide prediction. ISPRS Int J Geo-Inf 10:232. https://doi.org/10.3390/ijgi10040232

Hobbs PRN, Hallam JR, Forster A, Entwisle DC, Jones LD, Cripps AC, Northmore KJ, Self SJ, Meakin JK (2002) Engineering geology of British rocks and soils, Mudstones of the Mercia, Mudstone Group (Research report)

Hoek E, Bray JW (1981) Rock slope engineering, 3rd edition. ed. The Institute of Mining and Metallurgy, London, England
Hollick L, Shail R, Leveridge B (2006) Devonian rift-related sedimentation and Variscan tectonics – new data on the Looe and Gramscatho basins from the resurvey of the Newquay District. Presented at the Geosci. South-West England
Huang D, Song Y, Cen D, Fu G (2016) Numerical modeling of earthquake-induced landslide using an improved discontinuous deformation analysis considering dynamic friction degradation of joints. Rock Mech Rock Eng 49:4767–4786. https://doi.org/10.1007/s00603-016-1056-3
Huang SL, Yamasaki K (1993) Slope failure analysis using local minimum factor-of-safety approach. J Geotech Eng 119:1974–1989. https://doi.org/10.1061/(ASCE)0733-9410(1993)119:12(1974)
Hutchinson JN (1989) Morphological and geotechnical parameters of landslides in relation to geology and hydrogeology. Int J Rock Mech Min Sci Geomech Abstr 26:88. https://doi.org/10.1016/0148-9062(89)90310-0
Itasca Consulting Group Inc (2017) 3DEC | US Minneapolis - Itasca Consulting Group, Inc
Jing L (2003) A review of techniques, advances and outstanding issues in numerical modelling for rock mechanics and rock engineering. Int J Rock Mech Min Sci 40:283–353. https://doi.org/10.1016/S1365-1609(03)00013-3
Kemeny J (2003) The time-dependent reduction of sliding cohesion due to rock bridges along discontinuities: a fracture mechanics approach. Rock Mech Rock Eng 36:27–38. https://doi.org/10.1007/s00603-002-0032-2
Kveldsvik V, Einstein HH, Nilsen B, Blikra LH (2009) Numerical analysis of the 650,000 m^2 Åknes rock slope based on measured displacements and geotechnical data. Rock Mech Rock Eng 42:689–728. https://doi.org/10.1007/s00603-008-0005-1
Leveridge BE, Shail RK (2011) The Gramscatho Basin, south Cornwall, UK: Devonian active margin successions. Proc Geol Assoc 122:568–615. https://doi.org/10.1016/j.pgeola.2011.03.004
Liu C, Liu X, Peng X, Wang E, Wang S (2019) Application of 3D-DDA integrated with unmanned aerial vehicle–laser scanner (UAV-LS) photogrammetry for stability analysis of a blocky rock mass slope. Landslides 16:1645–1661. https://doi.org/10.1007/s10346-019-01196-6
Martin CD, Alzo'ubi AK, Cruden D (2011) Progressive failure mechanisms in a slope prone to toppling. Presented at the International Symposium on Rock Slope Stability in Open Pit Mining and Civil Engineering, Vancouver, Canada
Mousavi SZS, Tavakoli H, Moarefvand P, Rezaei M (2019) Assessing the effect of freezing-thawing cycles on the results of the triaxial compressive strength test for calc-schist rock. Int J Rock Mech Min Sci 123:104090. https://doi.org/10.1016/j.ijrmms.2019.104090
Robert McNeel and Associates (2012) Rhino
Schindelin J, Arganda-Carreras I, Frise E, Kaynig V, Longair M, Pietzsch T, Preibisch S, Rueden C, Saalfeld S, Schmid B, Tinevez J-Y, White DJ, Hartenstein V, Eliceiri K, Tomancak P, Cardona A (2012) Fiji: an open-source platform for biological-image analysis. Nat Methods 9:676–682. https://doi.org/10.1038/nmeth.2019
Shail RK, Coggan JS, Stead D (1998) Coastal landsliding in Cornwall, UK: mechanisms, modelling and implications. Presented at the 8th International Congress of the International-Association-for-Engineering-Geology-and-the-Environment, VANCOUVER, CANADA, pp 1323–1330
Shao C, Li Y, Lan H, Li P, Zhou R, Ding H, Yan Z, Dong S, Yan L, Deng T (2019) The role of active faults and sliding mechanism analysis of the 2017 Maoxian postseismic landslide in Sichuan. China Bull Eng Geol Environ 78:5635–5651. https://doi.org/10.1007/s10064-019-01480-8
Stead D (2021) ISRM. 34th ISRM Online Lect. https://www.isrm.net/gca/index.php?id=1588. Accessed 7 Jul 2021
Stead D, Eberhardt E, Coggan JS (2006) Developments in the characterization of complex rock slope deformation and failure using numerical modelling techniques. Eng Geol 83:217–235. https://doi.org/10.1016/j.enggeo.2005.06.033
Stead D, Wolter A (2015) A critical review of rock slope failure mechanisms: the importance of structural geology. J Struct Geol 74:1–23. https://doi.org/10.1016/j.jsg.2015.02.002
Travelletti J, Malet J-P, Samyn K, Grandjean G, Jaboyedoff M (2013) Control of landslide retrogression by discontinuities: evidence by the integration of airborne- and ground-based geophysical information. Landslides 10:37–54. https://doi.org/10.1007/s10346-011-0310-8
Vanneschi C, Eyre M, Venn A, Coggan JS (2019) Investigation and modeling of direct toppling using a three-dimensional distinct element approach with incorporation of point cloud geometry. Landslides 16:1453–1465. https://doi.org/10.1007/s10346-019-01192-w
Wang J, Zhang Y, Chen Y, Wang Q, Xiang C, Fu H, Wang P, Zhao JX, Zhao L (2021) Back-analysis of Donghekou landslide using improved DDA considering joint roughness degradation. Landslides. https://doi.org/10.1007/s10346-020-01586-1
Weidinger JT, Korup O, Munack H, Altenberger U, Dunning SA, Tippelt G, Lottermoser W (2014) Giant rockslides from the inside. Earth Planet Sci Lett 389:62–73. https://doi.org/10.1016/j.epsl.2013.12.017
Wu JH, Wang WN, Chang C-S, Wang CL (2005) Effects of strength properties of discontinuities on the unstable lower slope in the Chiu-fen-erh-shan landslide. Taiwan Eng Geol 78:173–186. https://doi.org/10.1016/j.enggeo.2004.12.005
Xia M, Chen G, Yu P, Peng X, Zou J (2021) Improvement of DDA with a new unified tensile fracture model for rock fragmentation and its application on dynamic seismic landslides. Rock Mech Rock Eng. https://doi.org/10.1007/s00603-020-02307-9
Zhang M, McSaveney M, Shao H, Zhang C (2018) The 2009 Jiweishan rock avalanche, Wulong, China: precursor conditions and factors leading to failure. Eng Geol 233:225–230. https://doi.org/10.1016/j.enggeo.2017.12.010

Lingfeng He (✉) · **John Coggan** · **Matthew Eyre**
Camborne School of Mines, University of Exeter, Penryn Campus, Penryn TR10 9EZ, UK
Email: lh640@exeter.ac.uk

Doug Stead
Department of Earth Sciences, Simon Fraser University, Vancouver, BC V5A 1S6, Canada

Mirko Francioni
Department of Pure and Applied Sciences, University of Urbino, Urbino, Italy